49th AIAA/ASME/ASCE/AHS/ASC Structures, Structural Dynamics, and Materials
7 - 10 April 2008, Schaumburg, IL

AIAA 2008-2092

Analysis of Composite Corrugated Panel Facesheet to Flange Joints

Phillip W. Yarrington[1] and Craig S. Collier[2]
Collier Research Corp., Hampton, VA, 23666

Brett A. Bednarcyk[3]
NASA Glenn Research Center, Cleveland, OH, 44235

This paper outlines a method for the stress analysis of bonded composite corrugated panel facesheet to flange joints. The method relies on the existing HyperSizer Joints software, which analyzes the bonded joint, along with a beam analogy model that provides the necessary boundary loading conditions to the joint analysis. The method is capable of predicting the full multiaxial stress and strain fields within the flange to facesheet joint and thus can determine margins and evaluate delamination. Results comparing the method to NASTRAN finite element model stress fields are provided.

I. Introduction

PRELIMINARY design of corrugated panels requires the rapid consideration of a wide range of panel configurations (materials, layups, facesheet thicknesses, stiffener geometries, etc.) to determine the optimum design for a given set of loads. To assess the efficiency of a given panel design, ply-level stresses are used in one or more failure criteria to estimate the panel design's minimum margin with respect to failure, given panel level loads. The standard method of determining ply-level stresses, finite element analysis, however, is not well suited for the rapid consideration of (sometimes) thousands of potential panel designs in which the geometry is not fixed. In contrast, the HyperSizer Structural Sizing Software[1] uses rapid, closed-form solution methods on the level of the panel, laminate, and ply to evaluate panel margins and determine the optimum lightweight design. This software still relies on a global finite element model to determine the panel level loads, but it calculates the internal stresses within the panel based on efficient analytical solutions.

The present paper is concerned with the local stresses that arise within the bonded joint that exists between the facesheet and stiffener flanges in a composite corrugated stiffened panel. Existing HyperSizer capabilities analyzed corrugated panels using the ply-level stresses in each component of such a stiffened panel (e.g., stresses in the flange, web, crown, and facesheet), but did not consider stress concentrations due to the facesheet-stiffener bond. To address this limitation, the methodology described herein combines an existing bonded joint analysis capability within the software with a beam analogy analysis of the corrugated panel geometry. The beam analogy analysis provides the boundary loads, which vary based on the panel configuration, to the joint analysis. The joint analysis then calculates ply-level in-plane and interlaminar stresses and adhesive stresses that arise in the joint between the facesheet and stiffeners, which can be used to determine ply-level margins. This new capability has been incorporated within HyperSizer, enabling sizing based on global load cases down to the level of the stress concentrations arising due to the bond of each stiffener in each panel. Results are presented that compare local stress concentrations predicted by HyperSizer to those predicted using continuum finite element models to represent the facesheet to stiffener flange joint of several corrugated panel configurations.

[1] Senior Research Engineer, 45 Diamond Hill Rd., AIAA Member, Phil.Yarrington@hypersizer.com
[2] Senior Research Engineer, AIAA Senior Member, Craig.Collier@hypersizer.com
[3] Materials Research Engineer, 21000 Brookpark Rd., 49-7, AIAA Senior Member, Brett.A.Bednarcyk@nasa.gov

II. Joint Analysis Model

The joint analysis model employed is based on Mortensen's unified stress analysis method[2,3], which has been extended and implemented in the HyperSizer Joints composite bonded joint analysis software. Extensions include accommodation of transverse in-plane straining, hygrothermal loads, computation of the local in-plane and interlaminar stresses throughout the adherends, accommodation of pressure loading, and delamination prediction[4-9]. Compared to other analytical (i.e., non-FEA) methods used for bonded joint analysis, the HyperSizer method is capable of handling more general situations, including various joint geometries, asymmetric and unbalanced laminates, and more general loading and boundary conditions. A wide range of joint types may be considered, and the adherends, which were originally modeled as classical laminates in cylindrical bending, are now considered to undergo 'generalized cylindrical bending', in which transverse straining is accommodated. Both linear and nonlinear behavior of an adhesive layer is admitted in the analysis. For linear analysis, the adhesive layer is modeled via a traction-separation law that responds similarly to the linear behavior cohesive elements within the ABAQUS finite element software[10]. This can be used to simulate a physical adhesive layer present in the joint, or, for cases without a non-negligible adhesive layer, the traction-separation model represents a zero-thickness cohesive layer that can be given a high penalty stiffness to hold the adherends together[11]. Inclusion of nonlinear adhesive behavior in the analysis is accomplished through the use of a secant modulus approach for the nonlinear tensile stress–strain relationship in conjunction with a yield criterion.

The equilibrium equations for each joint type are derived through direct imposition of force and moment equilibrium on joint elements, and by combination of the aforementioned equations and relations, a set of governing ordinary differential equations is obtained. The governing system of equations is solved numerically using Mortensen and Thomsen's[3] 'multi-segment method of integration,' yielding laminate-level fields and adhesive stresses that vary along the joint in each adherend. After the governing equations are solved, the ply-level in-plane stress components in the adherends can be calculated from Classical Lamination Theory (CLT). After solving for the in-plane stresses, the interlaminar stress components in the adherends are obtained through integration of the point-wise equilibrium equations. The details of HyperSizer's stress analysis method are described by Zhang et al.[5,8]. It is important to recognize that the HyperSizer joint analysis method is very efficient; the execution time for a typical problem is approximately 1/40 second. Furthermore, problem set up and post-processing is straightforward, enabling rapid consideration of a wide range of joint configurations for sizing optimization.

In order to model the flange to facesheet joint within a composite corrugated panel, appropriate boundary loading conditions must be applied within the HyperSizer Joints analysis. As shown in Fig. 1, the analysis domain for a hat stiffened panel is the flange and facesheet region, where the closed span and web attachments to the analysis domain are accounted for through the boundary loading conditions. This region is, in essence, a bonded doubler, which can be analyzed by HyperSizer Joints. A two sheet corrugated panel (which has continuous flanges between the hats) is shown in Fig. 2. The analysis region is again a bonded doubler. The next section describes the determination of the appropriate boundary loads to apply (BCs #2 and #3 in Fig. 1 and BCs #1 and #4 in Fig. 2) within the HyperSizer Joints analysis.

III. General Solution for Boundary Loads

The goal of this section is to determine the internal forces and moments in the components of a corrugated stiffened panel subjected to an applied shear force (V), an applied distributed load (force per unit length) due to internal pressure (P), and either an applied normal force (F) and moment (M) or a symmetry condition resulting in a normal reaction force (F) and moment (M) at point H, as shown in Fig. 3. Note that point H is the midpoint between the corrugations (see Fig. 3). For a two sheet corrugated panel, which has no open span, L_{os} is set to zero. A beam analogy model is used to determine the internal forces and moments, the knowledge of which provides the unknown applied boundary conditions indicated in Figs. 1 and 2. The two separate boundary conditions (applied force and moment vs. symmetry) are discussed in Sections III.A and III.B below. It should be notes that in the following beam analogy model, the direction along the facesheet is referred to as the x-direction (fig. 3), while in the joint analysis, this is the y-direction (Figs. 1 and 2).

In Fig. 3, member BD is referred to as the closed span (cs), member AB is referred to as the web (w), member AC is referred to as the crown (cr), member GB is referred to as the facesheet-flange combination (com), and member HG is referred to as the open span (os). Symmetry conditions are applied at points D and C that allow z-direction translation (w), but no x-direction translation (u) and no rotation. The model is restrained against w displacement at point B, the intersection between the hat flange and web. This choice was motivated by comparison to finite element analysis results for acreage deformation of a hat stiffened panel model subjected to pressure loading. Note that neither horizontal (x-direction) translation nor rotation is restrained at point B.

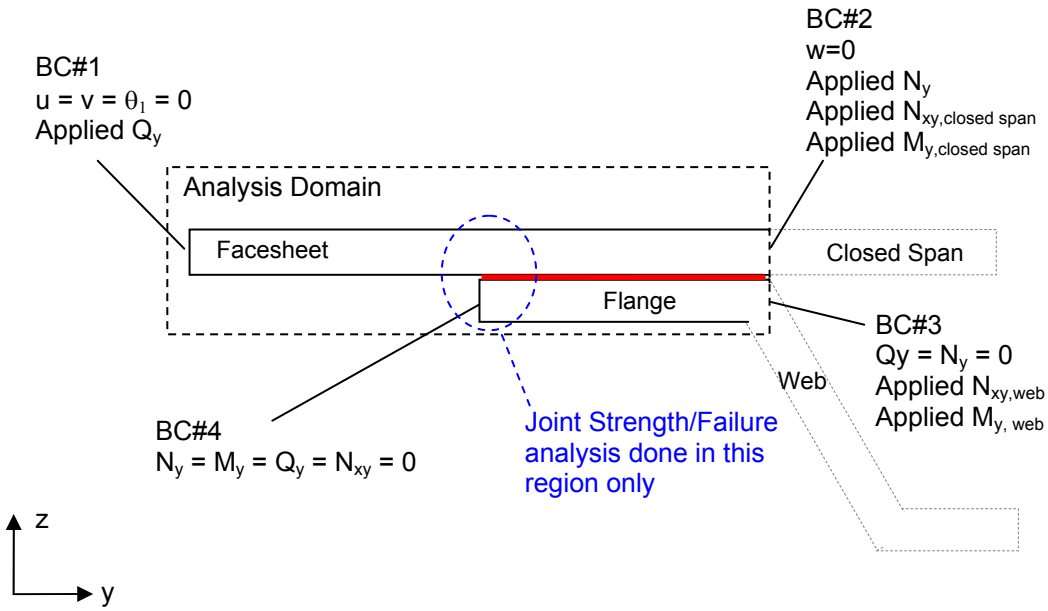

Fig. 1. Analysis geometry for a composite hat stiffened panel facesheet to flange joint.

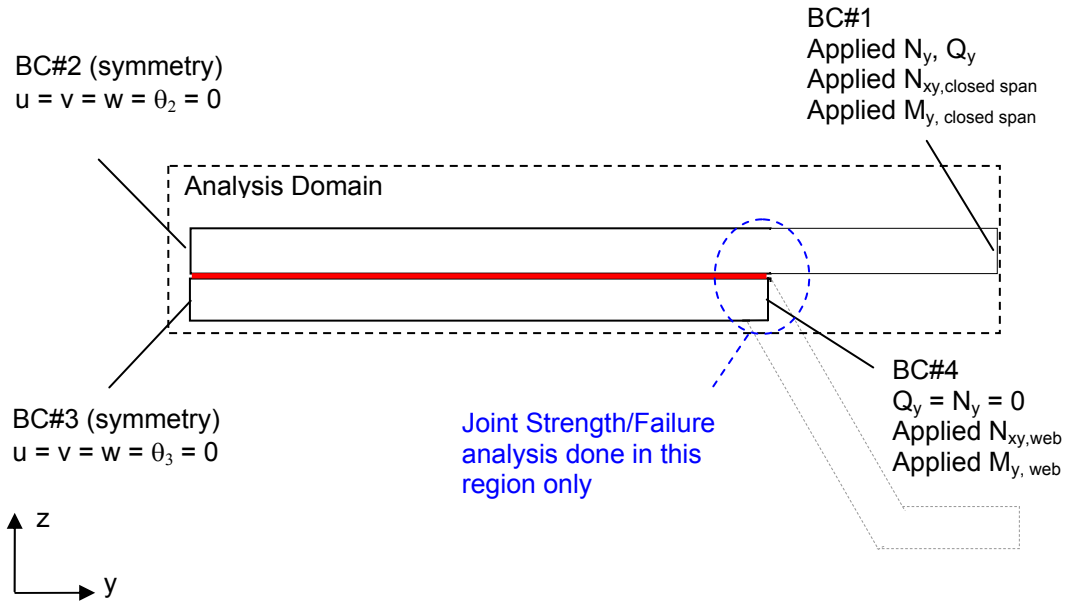

Fig. 2. Analysis geometry for a composite two sheet stiffened panel facesheet to flange joint.

A. Applied Force and Moment Boundary Conditions between Corrugations

A free body diagram of the analysis geometry is considered, as shown in Fig. 4. Applying global equilibrium,

$$\sum F_z = 0 \quad \rightarrow \quad B_z + \frac{S}{2}P - V = 0 \tag{1}$$

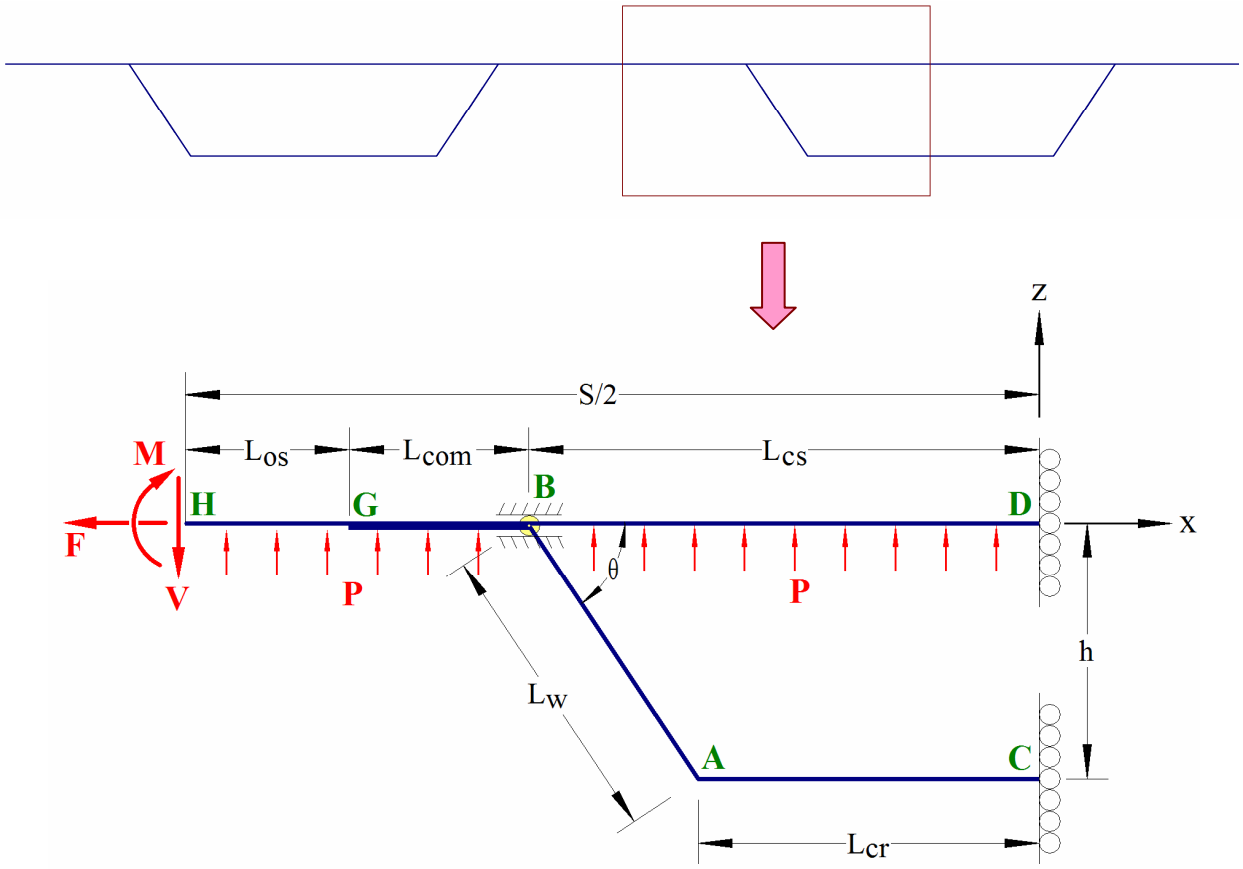

Fig. 3. Analysis geometry for a hat stiffened panel

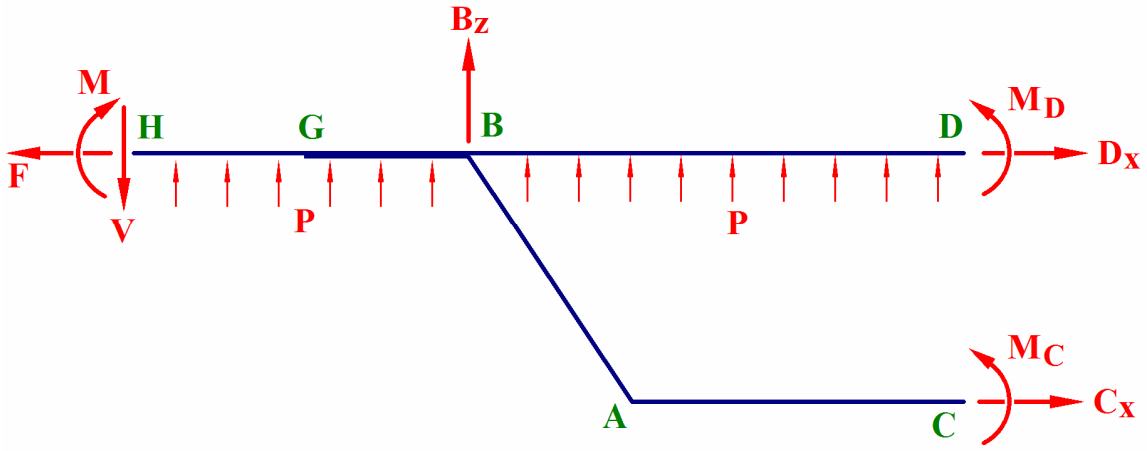

Fig. 4. Global free body diagram of the hat stiffened panel analysis geometry.

$$\sum F_x = 0 \quad \rightarrow \quad D_x - F + C_x = 0 \tag{2}$$

$$\sum M_{pt.\,D} = 0 \quad \rightarrow \quad M_D + M_C + hC_x + \frac{S}{2}V - \frac{S^2}{8}P - M - B_z L_{cs} = 0 \tag{3}$$

Substituting for B_z in Eq. (3) using Eq. (1),

$$M_D + M_C + hC_x + V\left(\frac{S}{2} - L_{cs}\right) + P\left(\frac{S}{2}L_{cs} - \frac{S^2}{8}\right) - M = 0 \tag{4}$$

Next a free body diagram of member HGBD is considered (as shown in Fig. 5), and equilibrium is applied,

$$\sum F_z = 0 \quad \rightarrow \quad B_z - BA_z + \frac{S}{2}P - V = 0 \tag{5}$$

$$\sum F_x = 0 \quad \rightarrow \quad D_x - F + BA_x = 0 \tag{6}$$

Combining Eqs. (5) and (1) gives,

$$BA_z = 0 \tag{7}$$

and combining Eqs. (6) and (2) gives,

$$BA_x = C_x \tag{8}$$

Therefore, equilibrium has established the relationship among the forces in the members, as well as one equation (4) relating the moments. Considering C_x, M_C, and M_D to be the unknown quantities in the formulation, two additional equations are needed in addition to Eq. (4). These equations will be obtained by applying beam theory deformation equations while imposing continuity of rotations and x-direction displacements at point B.

It is noted from the boundary condition at point D depicted in Fig. 3 that the x-direction displacement and the rotation of member BD at point D are zero. Considering the free body diagram of a section of member BD as shown in Fig. 6, and introducing a new $\hat{x}$ coordinate direction,

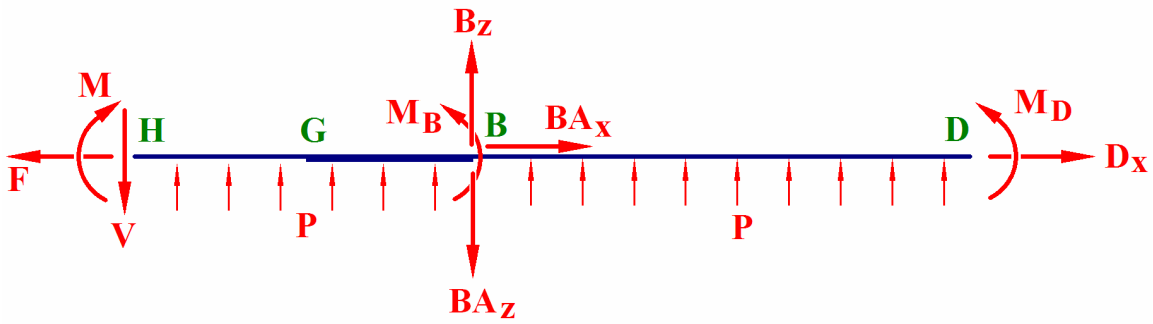

Fig. 5. Free body diagram of member HGBD (closed span, facesheet-flange combination, and open span)

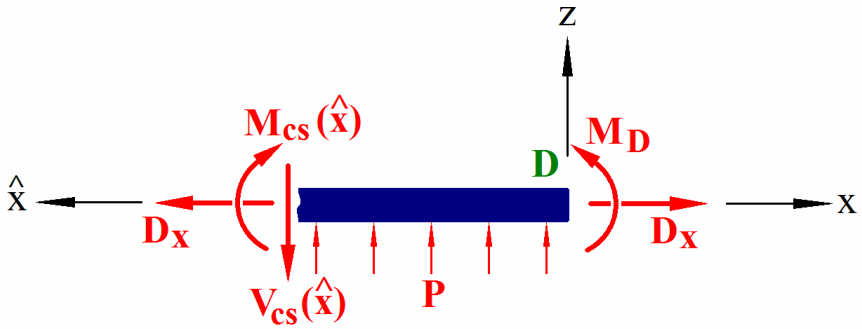

Fig. 6. Free body diagram of a section of member BD.

$$\sum F_z = 0 \quad \rightarrow \quad V_{cs} = P\,\hat{x} \tag{9}$$

$$\sum M_{pt.\,D} \quad \rightarrow \quad M_D - M_{cs} + V_{cs}\hat{x} - P\frac{\hat{x}^2}{2} = 0 \tag{10}$$

Combining Eqs. (9) and (10),

$$M_{cs} = M_D + P\frac{\hat{x}^2}{2} \tag{11}$$

Beam theory[12] enables the internal moment within the closed span to be related to the second derivative of the z-direction deformation (w) of the web as,

$$\frac{d^2 w(\hat{x})}{d\hat{x}^2} = \frac{M(\hat{x})}{E_{cs}\,I_{cs}} = \frac{1}{E_{cs}\,I_{cs}}\left[M_D + P\frac{\hat{x}^2}{2}\right] \tag{12}$$

where E_{cs} is the effective plane strain Young's modulus of the closed span in the x-direction, and I_{cs} is the area moment of inertia of the closed span face normal to the x-direction. Note that the plane strain Young's modulus differs from the standard Young's modulus by a factor of $(1-\nu_{xy}\,\nu_{yx})^{-1}$. For a composite laminate, this value can easily be determined from classical lamination theory. Integrating Eq. (12) and imposing the zero rotation boundary condition at point D gives,

$$\frac{dw(\hat{x})}{d\hat{x}} = \frac{1}{E_{cs}\,I_{cs}}\left[M_D\hat{x} + P\frac{\hat{x}^3}{6}\right] \tag{13}$$

which allows the rotation at point B (measured as positive in the clockwise direction) to be written as,

$$\frac{dw(\hat{x}=L_{cs})}{d\hat{x}} = \theta_B = \frac{M_D\,L_{cs}}{E_{cs}\,I_{cs}} + \frac{P\,L_{cs}^3}{6E_{cs}\,I_{cs}} \tag{14}$$

The axial (x-direction) deformation at point B is due to the axial force in member BD, and can be written as,

$$u_B = -\frac{D_x}{E_{cs}\,A_{cs}} L_{cs} = \frac{C_x - F}{E_{cs}\,A_{cs}} L_{cs} \tag{15}$$

where Eq. (2) has been employed.

Next, equations for the rotation and x-direction displacement at point B will be developed by considering the deformation of members AC (crown) and AB (web). Equating these expressions with Eqs. (14) and (15) will provide the two additional equations required to determine C_x, M_C, and M_D.

It is noted from Fig. 3 that, although the boundary condition at point C allows z-direction translation, no rotation is permitted at this point. Thus, the bending and rotation of member AC (crown) is due to the constant internal moment, M_C, while the axial deformation is due to the axial force, C_x (see Fig. 7). Therefore, the rotation, z-direction displacement, and axial displacement at point A can be written as[12],

$$\theta_A = \frac{M_C\,L_{cr}}{E_{cr}\,I_{cr}} \tag{16}$$

$$w_A = \frac{M_C L_{cr}^2}{2E_{cr}I_{cr}} + w_C \tag{17}$$

$$u_A = -\frac{C_x}{E_{cr}\,A_{cr}} L_{cr} \tag{18}$$

where E_{cr} is the effective plane strain Young's modulus of the crown in the x-direction, and I_{cr} is the area moment of inertia of the crown face normal to the x-direction, and w_C is the *z*-direction displacement at point C.

The web-crown combination (member BAC) is dismembered as shown in Fig. 8. A new, primed coordinate system is introduced for the web (member AB), with the x'-direction along the web (see Figs. 8 and 9). The section of member AB, shown in Fig. 10, is used to determine the internal moment, $M(x')$, by applying equilibrium,

$$\sum M_{pt.\,A} = 0 \quad \rightarrow \quad M_C - M(x') + C_x \sin(\theta)\,x' = 0 \tag{19}$$

Solving for the internal moment,

$$M(x') = M_C + C_x \sin(\theta)\,x' \tag{20}$$

Beam theory[10] enables the internal moment within the web to be related to the second derivative of the z'-direction deformation (w') of the web as,

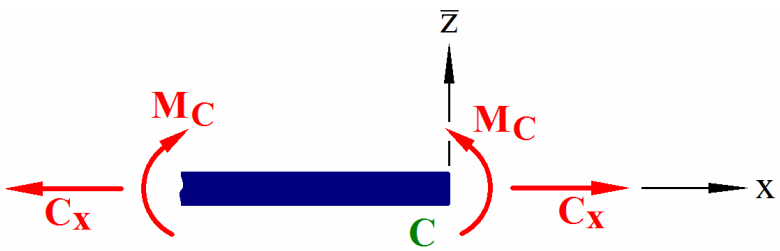

Fig. 7. Free body diagram of a section of member AC (crown).

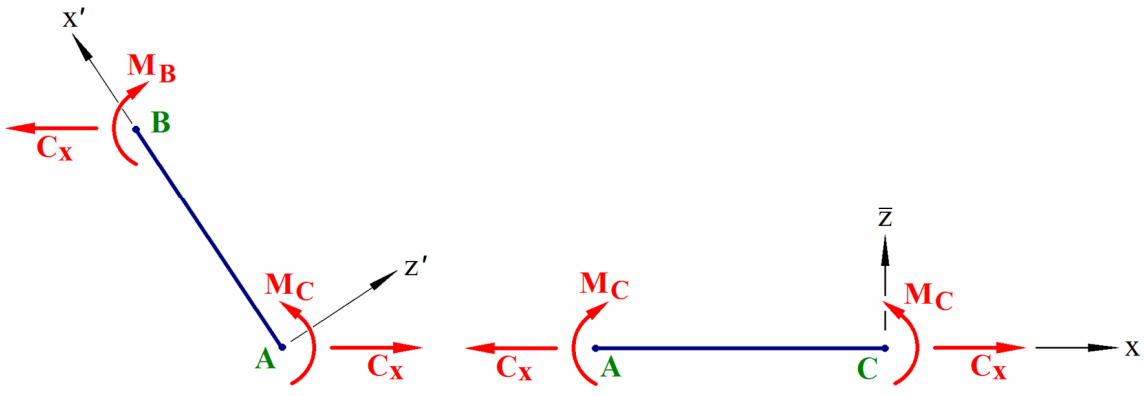

Fig. 8. Free body diagram of dismembered member BAC (crown and web).

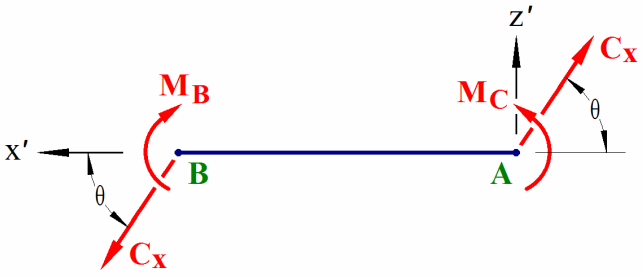

Fig. 9. Rotated free body diagram of member AB (web)

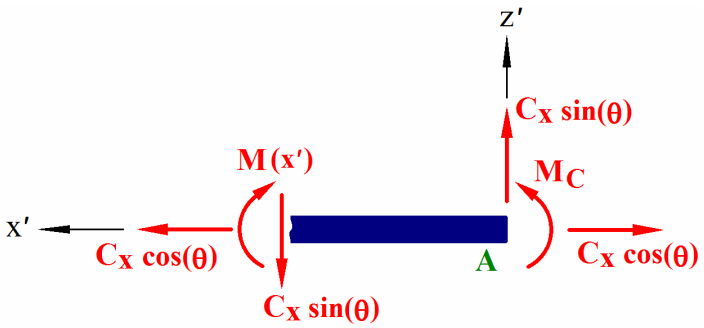

Fig. 10. Free body diagram of a section of member AB.

$$\frac{d^2 w'(x')}{dx'^2} = \frac{M(x')}{E_w I_w} = \frac{1}{E_w I_w}\left[M_C + C_x \sin(\theta) x'\right] \tag{21}$$

where E_w is the effective plane strain Young's modulus of the web in the x'-direction, and I_w is the area moment of inertia of the web face normal to the x'-direction. Integrating this expression provides the first derivative of w', which is equivalent to the rotation,

$$\frac{dw'(x')}{dx'} = \frac{1}{E_w I_w}\left[M_C x' + \frac{1}{2} C_x \sin(\theta) x'^2\right] + C_1 \tag{22}$$

where C_1 is a constant of integration, which is determined by imposing continuity of rotations at point A. Noting that a positive internal moment in the web will result in a positive (clockwise) rotation,

$$\theta_A = \frac{dw'(x'=0)}{dx'} = C_1 \tag{23}$$

Equating Eqs. (23) and (16),

$$C_1 = \frac{M_C L_{cr}}{E_{cr} I_{cr}} \tag{24}$$

Integrating Eq. (22) while employing Eq. (24) gives,

$$w'(x') = \frac{M_C}{2E_w I_w} x'^2 + \frac{C_x \sin(\theta)}{6E_w I_w} x'^3 + \frac{M_C L_{cr}}{E_{cr} I_{cr}} x' + C_2 \tag{25}$$

where C_2 is a constant of integration, which is found in terms of the web z'-direction deformation at point A, w'_A,

$$w'(x'=0) = w'_A = C_2 \tag{26}$$

Similarly, the axial deformation of the web is written as,

$$u'(x') = \frac{C_x \cos(\theta)}{E_w A_w} x' + u'_A \tag{27}$$

where u'_A is the web x'-direction deformation at point A. The rotation equations relating the web primed coordinate system deformation and the unprimed coordinate system deformations are given by,

$$\begin{aligned} u' &= -u \cos(\theta) + w \sin(\theta) \\ w' &= u \sin(\theta) + w \cos(\theta) \end{aligned} \tag{28}$$

Therefore, from equations (25) – (28), we have,

$$w'(x') = \frac{M_C}{2E_w I_w} x'^2 + \frac{C_x \sin(\theta)}{6E_w I_w} x'^3 + \frac{M_C L_{cr}}{E_{cr} I_{cr}} x' + u_A \sin(\theta) + w_A \cos(\theta) \tag{29}$$

$$u'(x') = \frac{C_x \cos(\theta)}{E_w A_w} x' - u_A \cos(\theta) + w_A \sin(\theta) \tag{30}$$

Inverting Eq. (28) yields,

$$\begin{aligned} u &= -u' \cos(\theta) + w' \sin(\theta) \\ w &= u' \sin(\theta) + w' \cos(\theta) \end{aligned} \tag{31}$$

which enables the x-direction deformation of the web at point B to be written as,

$$u_B = -u'_B\cos(\theta) + w'_B\sin(\theta) = -u'(x' = L_w)\cos(\theta) + w'(x' = L_w)\sin(\theta)$$
$$= -\frac{C_x\cos^2(\theta)}{E_w A_w}L_w + u_A\cos^2(\theta) - w_A\sin(\theta)\cos(\theta) + \frac{M_C\sin(\theta)}{2E_w I_w}L_w^2 + \tag{32}$$
$$\frac{C_x\sin^2(\theta)}{6E_w I_w}L_w^3 + \frac{M_C L_{cr}\sin(\theta)}{E_{cr} I_{cr}}L_w + u_A\sin^2(\theta) + w_A\cos(\theta)\sin(\theta)$$

Recognizing that $\sin^2(\theta) + \cos^2(\theta) = 1$ and substituting for u_A in Eq. (32) using Eq. (18) gives,

$$u_B = -\frac{C_x\cos^2(\theta)}{E_w A_w}L_w + \frac{M_C\sin(\theta)}{2E_w I_w}L_w^2 + \frac{C_x\sin^2(\theta)}{6E_w I_w}L_w^3 + \frac{M_C L_{cr}\sin(\theta)}{E_{cr} I_{cr}}L_w - \frac{C_x L_{cr}}{E_{cr} A_{cr}} \tag{33}$$

Equating Eq. (33) with the expression for u_B determined from member BD, Eq. (15),

$$-\frac{C_x\cos^2(\theta)}{E_w A_w}L_w + \frac{M_C\sin(\theta)}{2E_w I_w}L_w^2 + \frac{C_x\sin^2(\theta)}{6E_w I_w}L_w^3 + \frac{M_C L_{cr}\sin(\theta)}{E_{cr} I_{cr}}L_w - \frac{C_x L_{cr}}{E_{cr} A_{cr}} = \frac{C_x - F}{E_{cs} A_{cs}}L_{cs} \tag{34}$$

Noting that the internal moment within the web will cause a positive (clockwise) rotation at point B, equations (22) and (24) can be used to write the web rotation at point B as,

$$\frac{dw'(x' = L_w)}{dx'} = \theta_B = \frac{M_C L_w}{E_w I_w} + \frac{C_x\sin(\theta)L_w^2}{2E_w I_w} + \frac{M_C L_{cr}}{E_{cr} I_{cr}} \tag{35}$$

Equating Eq. (35) with the expression for θ_B determined from member BD, Eq. (14), gives,

$$\frac{M_C L_w}{E_w I_w} + \frac{C_x\sin(\theta)L_w^2}{2E_w I_w} + \frac{M_C L_{cr}}{E_{cr} I_{cr}} = \frac{M_D L_{cs}}{E_{cs} I_{cs}} + \frac{P L_{cs}^3}{6E_{cs} I_{cs}} \tag{36}$$

Equations (4), (36), and (34) now form three algebraic equations for the three unknown quantities, C_x, M_C, and M_D. Reiterating these equations, we have:

Equilibrium

$$M_D + M_C + hC_x + V\left(\frac{S}{2} - L_{cs}\right) + P\left(\frac{S}{2}L_{cs} - \frac{S^2}{8}\right) - M = 0 \tag{37}$$

Rotation Continuity at Point B

$$\frac{M_C L_w}{E_w I_w} + \frac{C_x\sin(\theta)L_w^2}{2E_w I_w} + \frac{M_C L_{cr}}{E_{cr} I_{cr}} = \frac{M_D L_{cs}}{E_{cs} I_{cs}} + \frac{P L_{cs}^3}{6E_{cs} I_{cs}} \tag{38}$$

x-Displacement Continuity at Point B

$$-\frac{C_x\cos^2(\theta)}{E_w A_w}L_w + \frac{M_C\sin(\theta)}{2E_w I_w}L_w^2 + \frac{C_x\sin^2(\theta)}{6E_w I_w}L_w^3 + \frac{M_C L_{cr}\sin(\theta)}{E_{cr} I_{cr}}L_w - \frac{C_x L_{cr}}{E_{cr} A_{cr}} = \frac{C_x - F}{E_{cs} A_{cs}}L_{cs} \tag{39}$$

To solve these three equations, we rewrite Eq. (39) as,

$$C_x \underbrace{\left[-\frac{L_w \cos^2(\theta)}{E_w A_w} + \frac{L_w^3 \sin^2(\theta)}{6E_w I_w} - \frac{L_{cr}}{E_{cr} A_{cr}} - \frac{L_{cs}}{E_{cs} A_{cs}} \right]}_{K_1} + M_C \underbrace{\left[\frac{L_w^2 \sin(\theta)}{2E_w I_w} + \frac{L_w L_{cr} \sin(\theta)}{E_{cr} I_{cr}} \right]}_{K_2} = \underbrace{\frac{-FL_{cs}}{E_{cs} A_{cs}}}_{B_1} \quad (40)$$

and identify the terms,

$$K_1 = -\frac{L_w \cos^2(\theta)}{E_w A_w} + \frac{L_w^3 \sin^2(\theta)}{6E_w I_w} - \frac{L_{cr}}{E_{cr} A_{cr}} - \frac{L_{cs}}{E_{cs} A_{cs}} \quad (41)$$

$$K_2 = \frac{L_w^2 \sin(\theta)}{2E_w I_w} + \frac{L_w L_{cr} \sin(\theta)}{E_{cr} I_{cr}} \quad (42)$$

$$B_1 = \frac{-FL_{cs}}{E_{cs} A_{cs}} \quad (43)$$

Thus, from Eq. (40), we have,

$$M_C = \frac{B_1}{K_2} - C_x \frac{K_1}{K_2} \quad (44)$$

Similarly, Eq. (38) can be written as,

$$M_C \underbrace{\left[\frac{L_w}{E_w I_w} + \frac{L_{cr}}{E_{cr} I_{cr}} \right]}_{K_3} + C_x \underbrace{\left[\frac{L_w^2 \sin(\theta)}{2E_w I_w} \right]}_{K_4} = M_D \underbrace{\left[\frac{L_{cs}}{E_{cs} I_{cs}} \right]}_{K_5} + \underbrace{\frac{P L_{cs}^3}{6E_{cs} I_{cs}}}_{B_2} \quad (45)$$

with the following terms identified,

$$K_3 = \frac{L_w}{E_w I_w} + \frac{L_{cr}}{E_{cr} I_{cr}} \quad (46)$$

$$K_4 = \frac{L_w^2 \sin(\theta)}{2E_w I_w} \quad (47)$$

$$K_5 = \frac{L_{cs}}{E_{cs} I_{cs}} \quad (48)$$

$$B_2 = \frac{P L_{cs}^3}{6E_{cs} I_{cs}} \quad (49)$$

Thus, from Eq. (45) combined with Eq. (44) we have,

$$M_D = C_x\left[\frac{K_4}{K_5} - \frac{K_1 K_3}{K_2 K_5}\right] + \frac{B_1 K_3}{K_2 K_5} - \frac{B_2}{K_5} \tag{50}$$

Substituting Eqs. (50) and (44) into the equilibrium equation (37) gives,

$$C_x\left[\frac{K_4}{K_5} - \frac{K_1 K_3}{K_2 K_5}\right] + \frac{B_1 K_3}{K_2 K_5} - \frac{B_2}{K_5} + \frac{B_1}{K_2} - C_x\frac{K_1}{K_2} + hC_x + V\left(\frac{S}{2} - L_{cs}\right) + P\left(\frac{S}{2}L_{cs} - \frac{S^2}{8}\right) - M = 0 \tag{51}$$

which can be solved for C_x in terms of known quantities,

$$C_x = \frac{M + P\left(\frac{S^2}{8} - \frac{S}{2}L_{cs}\right) + V\left(L_{cs} - \frac{S}{2}\right) - \frac{B_1}{K_2}\left(\frac{K_3}{K_5} + 1\right) + \frac{B_2}{K_5}}{\frac{K_4}{K_5} - \frac{K_1 K_3}{K_2 K_5} - \frac{K_1}{K_2} + h} \tag{52}$$

The remaining unknowns, M_C and M_D, can then be determined from Eqs. (44) and (50).

The forces and moments in each component are given in terms of the three unknowns as follows,

$$F_{cs} = F - C_x \tag{53}$$

$$V_{cs} = P\hat{x} \tag{54}$$

$$M_{cs} = M_D + \frac{P\hat{x}^2}{2} \tag{55}$$

$$F_{cr} = C_x \tag{56}$$

$$V_{cr} = 0 \tag{57}$$

$$M_{cr} = M_C \tag{58}$$

$$F_w = C_x\cos(\theta) \tag{59}$$

$$V_w = C_x\sin(\theta) \tag{60}$$

$$M_w = M_C + C_x\sin(\theta)\, x' \tag{61}$$

where F_i denotes an axial force and V_i denotes a shear force. It is noted that the crown has constant axial force and moment and zero shear force, the web has constant axial and shear force and a linear moment, and the closed span has constant axial force, linear shear force, and quadratic moment.

It should be noted that the areas and moments of inertia of each component are linearly dependent on the out-of-plane dimension of the hat (i.e., the dimension in the y-direction in Fig. 3). However, examining Eqs. (37) – (39), it is clear that this dimension drops out the governing equations. Thus, it can be concluded that if the applied moment, *M*, applied shear force, *V*, and applied axial force, *F*, are given as force and moment resultants rather than a moment and forces, and the distributed force due to pressure is given as a true pressure rather than a force per unit length, the force and moment solutions in Eqs. (53) – (61) will be resultants as well.

B. Symmetry Boundary Condition between Corrugations

Next a symmetry boundary condition is considered at the midpoint between the panel corrugations, point H in Fig. 11. The corresponding free body diagram is identical to that shown in Fig. 4. In this case, the normal force and moment at point H are unknown reactions, while the shear force at point H is a known applied load. The primary

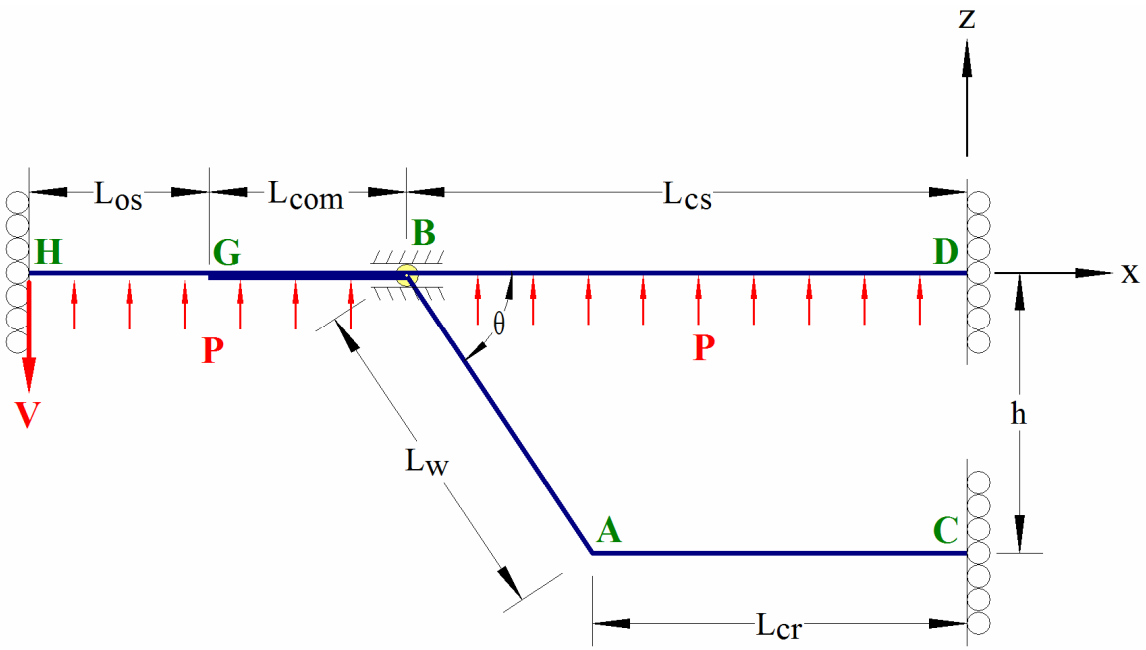

Fig. 11. Analysis geometry for a hat stiffened panel – symmetry at point H.

distinction from the derivation in the previous section is that the deformation of the open span and face-sheet flange combination must now be considered in order to determine the unknown reactions at point H.

A free body diagram of a section of member HGB is shown in Fig. 12, where *j* takes on the value of "os" or "com" depending on whether the section cut is taken within the open span or flange/facesheet combination. A new $\tilde{x}$ coordinate direction has been introduced. Applying equilibrium,

$$\sum F_z = 0 \quad \rightarrow \quad V_j = V - P\tilde{x} \tag{62}$$

$$\sum M_{pt.H} \quad \rightarrow \quad M_j + P\frac{\tilde{x}^2}{2} - M + V_j\tilde{x} = 0 \tag{63}$$

Substituting Eq. (62) into Eq. (63) gives,

$$M_j = M + P\frac{\tilde{x}^2}{2} - V\tilde{x} \tag{64}$$

Once again utilizing beam theory[12], the second derivative of the z-direction deformation within the open span can be written as,

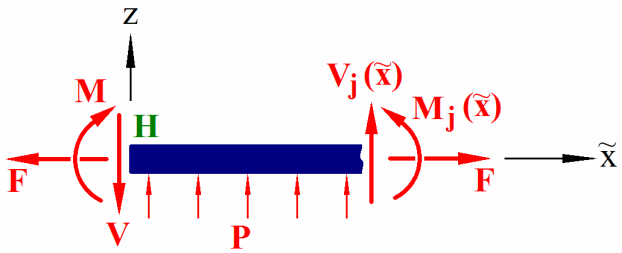

Fig. 12. Free body diagram of a section of member HGB.

$$\frac{d^2 w_{os}\left(\tilde{x}\right)}{d\tilde{x}^2} = \frac{M_{os}\left(\tilde{x}\right)}{E_{os}\, I_{os}} = \frac{1}{E_{os}\, I_{os}}\left[M + P\frac{\tilde{x}^2}{2} - V\tilde{x}\right] \tag{65}$$

Integrating Eq. (65) and imposing the zero rotation boundary condition at point H ($\tilde{x} = 0$) gives,

$$\frac{dw_{os}\left(\tilde{x}\right)}{d\tilde{x}} = \frac{1}{E_{os}\, I_{os}}\left[M\tilde{x} + P\frac{\tilde{x}^3}{6} - V\frac{\tilde{x}^2}{2}\right] \tag{66}$$

which allows the rotation at point G (measured as positive in the clock-wise direction) to be written as,

$$\frac{dw_{os}\left(\tilde{x} = L_{os}\right)}{d\tilde{x}} = -\theta_G = \frac{ML_{os}}{E_{os}\, I_{os}} + \frac{PL_{os}^3}{6E_{os}\, I_{os}} - \frac{VL_{os}^2}{2E_{os}\, I_{os}} \tag{67}$$

Similarly, applying beam theory[12] to the flange/facesheet combination gives,

$$\frac{d^2 w_{com}\left(\tilde{x}\right)}{d\tilde{x}^2} = \frac{M_{com}\left(\tilde{x}\right)}{E_{com}\, I_{com}} = \frac{1}{E_{com}\, I_{com}}\left[M + P\frac{\tilde{x}^2}{2} - V\tilde{x}\right] \tag{68}$$

Integrating Eq. (68),

$$\frac{dw_{com}\left(\tilde{x}\right)}{d\tilde{x}} = \frac{M\tilde{x}}{E_{com}\, I_{com}} + \frac{P\tilde{x}^3}{6E_{com}\, I_{com}} - \frac{V\tilde{x}^2}{2E_{com}\, I_{com}} + \tilde{C} \tag{69}$$

where $\tilde{C}$ is a constant of integration which can be determined by applying Eq. (69) to determine the rotation at point G (measured as positive in the clock-wise direction),

$$\frac{dw_{com}\left(\tilde{x} = L_{os}\right)}{d\tilde{x}} = -\theta_G = \frac{ML_{os}}{E_{com}\, I_{com}} + \frac{PL_{os}^3}{6E_{com}\, I_{com}} - \frac{VL_{os}^2}{2E_{com}\, I_{com}} + \tilde{C} \tag{70}$$

and equating Eqs. (70) and (67),

$$\tilde{C} = \frac{ML_{os}}{E_{os}\, I_{os}} + \frac{PL_{os}^3}{6E_{os}\, I_{os}} - \frac{VL_{os}^2}{2E_{os}\, I_{os}} - \frac{ML_{os}}{E_{com}\, I_{com}} - \frac{PL_{os}^3}{6E_{com}\, I_{com}} + \frac{VL_{os}^2}{2E_{com}\, I_{com}} \tag{71}$$

The rotation at point B (measured as positive in the clock-wise direction) can then be written as,

$$\frac{dw_{com}\left(\tilde{x} = L_{os} + L_{com}\right)}{d\tilde{x}} = -\theta_B = \frac{M\left(L_{os} + L_{com}\right)}{E_{com}\, I_{com}} + \frac{P\left(L_{os} + L_{com}\right)^3}{6E_{com}\, I_{com}} - \frac{V\left(L_{os} + L_{com}\right)^2}{2E_{com}\, I_{com}} + \tilde{C} \tag{72}$$

Substituting Eq. (71) into Eq. (72),

$$\theta_B = M\underbrace{\left[-\frac{L_{os}}{E_{os}I_{os}}-\frac{L_{com}}{E_{com}I_{com}}\right]}_{K_6}+\underbrace{\frac{P}{6}\left[-\frac{\left(L_{os}+L_{com}\right)^3-L_{os}^3}{E_{com}I_{com}}-\frac{L_{os}^3}{E_{os}I_{os}}\right]+\frac{V}{2}\left[\frac{\left(L_{os}+L_{com}\right)^2-L_{os}^2}{E_{com}I_{com}}+\frac{VL_{os}^2}{E_{os}I_{os}}\right]}_{B_3} \tag{73}$$

with the following terms identified,

$$K_6 = -\frac{L_{os}}{E_{os}I_{os}}-\frac{L_{com}}{E_{com}I_{com}} \tag{74}$$

$$B_3 = \frac{P}{6}\left[-\frac{\left(L_{os}+L_{com}\right)^3-L_{os}^3}{E_{com}I_{com}}-\frac{L_{os}^3}{E_{os}I_{os}}\right]+\frac{V}{2}\left[\frac{\left(L_{os}+L_{com}\right)^2-L_{os}^2}{E_{com}I_{com}}+\frac{VL_{os}^2}{E_{os}I_{os}}\right] \tag{75}$$

Equation (73) can then be written as,

$$\theta_B = MK_6 + B_3 \tag{76}$$

while Eq. (14) can be written as,

$$\theta_B = M_D K_5 + B_2 \tag{77}$$

where Eqs. (48) and (49) have been used. Equating Eqs. (76) and (77) gives,

$$M = M_D\frac{K_5}{K_6}+\frac{B_2}{K_6}-\frac{B_3}{K_6} \tag{78}$$

Substituting Eq. (78) into Eq. (37) provides the replacement for the equilibrium equation in terms of the three unknowns, C_x, M_C, and M_D,

Equilibrium

$$M_D\left(1-\frac{K_5}{K_6}\right)+M_C+hC_x+V\left(\frac{S}{2}-L_{cs}\right)+P\left(\frac{S}{2}L_{cs}-\frac{S^2}{8}\right)-\frac{B_2}{K_6}+\frac{B_3}{K_6}=0 \tag{79}$$

Noting from Fig. 4 that the axial force in member HGB is constant and equal to *F*, the axial displacement at point G can be related to that at point B as,

$$u_G = u_B - F\left(\frac{L_{com}}{E_{com}A_{com}}\right) \tag{80}$$

while the axial displacement at point H can be related to that at point G as,

$$u_H = u_G - F\left(\frac{L_{os}}{E_{os}A_{os}}\right) \tag{81}$$

Substituting the expression for u_B obtained from the closed span, Eq. (15), into Eq. (80) and the result into Eq. (81) yields,

$$u_H = C_x \frac{L_{cs}}{E_{cs}A_{cs}} - F\frac{L_{cs}}{E_{cs}A_{cs}} - F\frac{L_{com}}{E_{com}A_{com}} - F\frac{L_{os}}{E_{os}A_{os}} = 0 \tag{82}$$

where the zero axial displacement boundary condition at point H (see Fig. 11) has been imposed. Solving Eq. (82) for F yields,

$$F = C_x \underbrace{\left(\frac{\dfrac{L_{cs}}{E_{cs}A_{cs}}}{\dfrac{L_{cs}}{E_{cs}A_{cs}} + \dfrac{L_{com}}{E_{com}A_{com}} + \dfrac{L_{os}}{E_{os}A_{os}}} \right)}_{K_7} \tag{83}$$

or

$$F = C_x K_7 \tag{84}$$

with

$$K_7 = \frac{\dfrac{L_{cs}}{E_{cs}A_{cs}}}{\dfrac{L_{cs}}{E_{cs}A_{cs}} + \dfrac{L_{com}}{E_{com}A_{com}} + \dfrac{L_{os}}{E_{os}A_{os}}} \tag{85}$$

Substituting Eq. (84) into Eq. (39) provides the replacement for Eq. (39),

x-Displacement Continuity at Point B

$$\begin{aligned} &-\frac{C_x \cos^2(\theta)}{E_w A_w} L_w + \frac{M_C \sin(\theta)}{2E_w I_w} L_w^2 + \frac{C_x \sin^2(\theta)}{6E_w I_w} L_w^3 + \frac{M_C L_{cr} \sin(\theta)}{E_{cr} I_{cr}} L_w - \frac{C_x L_{cr}}{E_{cr} A_{cr}} \\ &= \frac{C_x}{E_{cs} A_{cs}} L_{cs} - \frac{C_x K_7}{E_{cs} A_{cs}} L_{cs} \end{aligned} \tag{86}$$

The rotation continuity equation (38) remains valid.

To solve Eqs. (79), (86), and (38) for the three unknowns, C_x, M_C, and M_D, Eq. (86) is rewritten as,

$$C_x K_1 + M_C K_2 = \frac{-C_x K_7 L_{cs}}{E_{cs} A_{cs}} \tag{87}$$

where Eqs. (41) and (42) have been employed. Upon rearrangement, Eq. (87) becomes,

$$C_x \underbrace{\left(K_1 + \frac{K_7 L_{cs}}{E_{cs} A_{cs}} \right)}_{K_1'} + M_C K_2 = \underbrace{0}_{B_1'} \tag{88}$$

and replaces Eq. (44) when written in the form,

$$M_C = \frac{B_1'}{K_2} - C_x \frac{K_1'}{K_2} \tag{89}$$

with,

$$K_1' = K_1 + \frac{K_7 L_{cs}}{E_{cs}\, A_{cs}} \tag{90}$$

and,

$$B_1' = 0 \tag{91}$$

Substituting Eq. (89) into Eq. (45),

$$M_D = C_x \left[\frac{K_4}{K_5} - \frac{K_1' K_3}{K_2 K_5} \right] + \frac{B_1' K_3}{K_2 K_5} - \frac{B_2}{K_5} \tag{92}$$

Substituting Eq. (92) into Eq. (78), the unknown reaction moment at point H can be written as a function of C_x,

$$M = C_x \left[\frac{K_4}{K_6} - \frac{K_1' K_3}{K_2 K_6} \right] + \frac{B_1' K_3}{K_2 K_6} - \frac{B_3}{K_6} \tag{93}$$

Substituting Eqs. (92), and (89) into the equilibrium equation (79),

$$\begin{aligned} &C_x \left[\frac{K_4}{K_5} - \frac{K_1' K_3}{K_2 K_5} \right] + \frac{B_1' K_3}{K_2 K_5} - \frac{B_2}{K_5} + \frac{B_1'}{K_2} - C_x \frac{K_1'}{K_2} + hC_x + V\left(\frac{S}{2} - L_{cs} \right) + P\left(\frac{S}{2} L_{cs} - \frac{S^2}{8} \right) \\ &-C_x \left[\frac{K_4}{K_6} - \frac{K_1' K_3}{K_2 K_6} \right] - \frac{B_1' K_3}{K_2 K_6} + \frac{B_3}{K_6} = 0 \end{aligned} \tag{94}$$

This equation replaces Eq. (51) and can be solved for C_x,

$$C_x = \frac{P\left(\frac{S^2}{8} - \frac{S}{2} L_{cs} \right) + V\left(L_{cs} - \frac{S}{2} \right) - \frac{B_1'}{K_2}\left(\frac{K_3}{K_5} + 1 + \frac{K_3}{K_6} \right) + \frac{B_2}{K_5} - \frac{B_3}{K_6}}{\frac{K_4}{K_5} - \frac{K_1' K_3}{K_2 K_5} - \frac{K_1'}{K_2} + h - \frac{K_4}{K_6} + \frac{K_1' K_3}{K_2 K_6}} \tag{95}$$

Equation (95) replaces Eq. (52) for the present case where symmetry is specified at point H (see Fig. 11) and the reaction normal force, F, and moment at point H, M, are unknown. Once C_x is determined, F can be calculated from Eq. (84) and M can be calculated from Eq. (93).

The forces and moments in the open span and facesheet-flange combination are given by,

$$F_{com} = F_{os} = F \tag{96}$$

$$V_{com} = V_{os} = V - P\tilde{x} \tag{97}$$

$$M_{com} = M_{os} = M - V\tilde{x} + \frac{P\tilde{x}^2}{2} \tag{98}$$

It should be noted that Eqs. (96) – (98) are valid for the applied force and moment boundary conditions described in section III.A.

IV. Results and Discussion

Five verification examples are presented below comparing the current solution within HyperSizer to NASTRAN finite element stress results. The first four cases consider hat stiffened and two sheet corrugated panels, with isotropic adherends, subjected to tensile and moment loads at point H. A final example then considers a composite hat stiffened panel subjected to internal pressure with the symmetry condition applied at point H.

A. Example 1: Hat Panel Loaded with Tensile Force

The first example problem considers a hat stiffened panel subjected to a tensile force resultant of 1 lb/in transverse to the direction of the hat stiffeners. It is assumed that the hat stiffeners are bonded to the face sheet with an epoxy adhesive. The problem dimensions and isotropic material properties are summarized in Fig. 13. Fig. 14 shows a plane strain NASTRAN finite element model of the problem, illustrating the deformed shape. The resulting shear stress, τ_{yz}, within the facesheet to flange joint region is shown in Fig. 15a. Fig. 15b compares the shear stress plotted along the middle of the adhesive (dashed line in Fig. 15a) in the finite element solution with the HyperSizer Joints adhesive shear stress solution. As shown, the agreement is excellent.

Variable Designs	
	Value
Unit Weight (lb / ft^2)	3.493
Top Face - Thickness (in)	0.1
Core Web - Thickness (in)	0.09
Bottom Face - Thickness (in)	0
Panel - Height (in)	1.747
Corrugation - Spacing (in)	4
Bottom Crown - Width (in)	0.8
Core Web - Angle (degrees)	82.24
Top Flange - Width, hat only (in)	2.079
Top Clear Span - Free Width (in)	0.6969
Top Flange - Thickness (in)	0.09
Bottom Crown - Thickness (in)	0.09

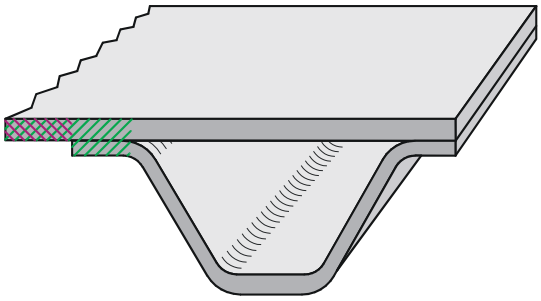

Conceptual Hat Stiffened Panel Geometry

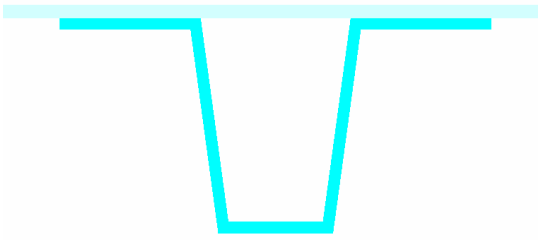

To-Scale Hat Stiffened Panel

Facesheet and Hat: Aluminum
E = 10 Msi
G = 3.846 Msi
ν = 0.3

Adhesive: Epoxy
E = .445 Msi
G = .165 Msi
ν = 0.35
thickness = 0.009”

Fig. 13. Example 1 and 2 hat stiffened panel parameters.

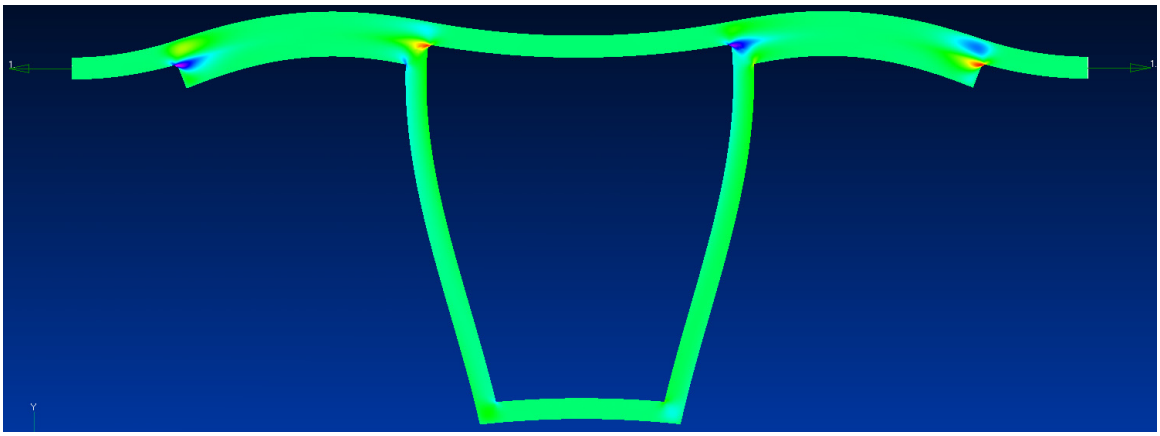

Fig. 14. NASTRAN finite element model deformed shape for example 1 hat stiffened panel.

(a)

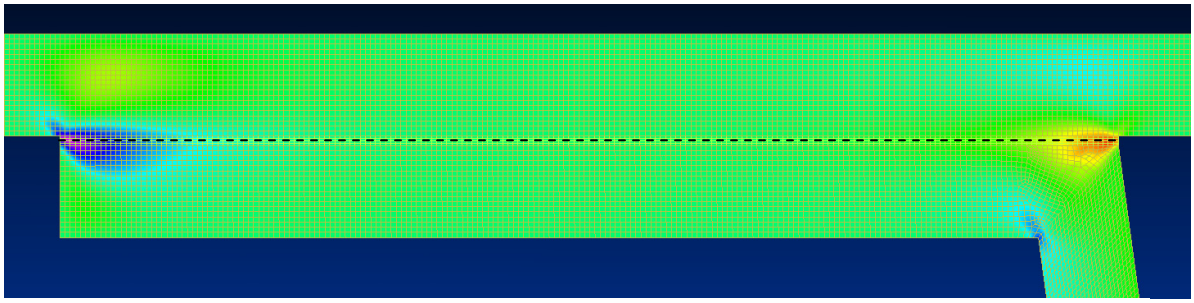

(b)

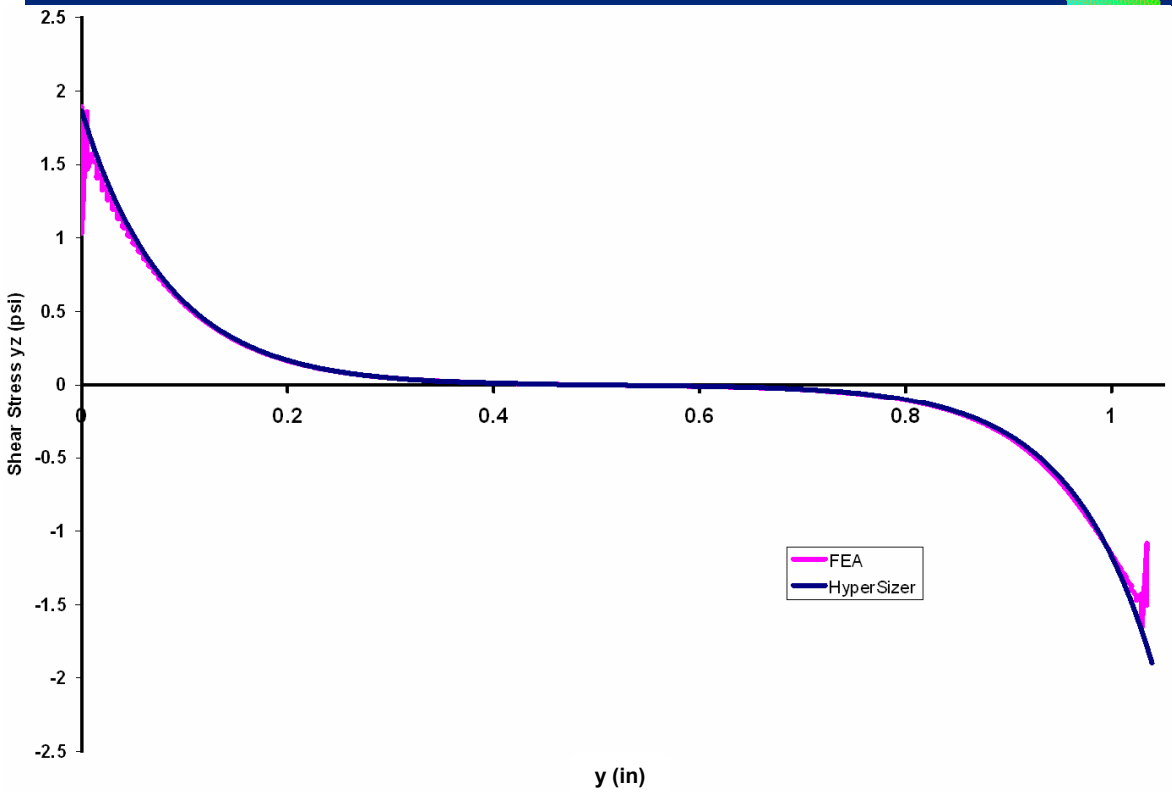

Fig. 15. Shear stress, τ_{yz}, (a) in NASTRAN finite element model (b) plotted along adhesive (dashed line in a), comparing finite element model with HyperSizer Joints.

Fig. 16a shows the peel stress field in the finite element model solution, while Fig. 16b compares the peel stress along the adhesive (dashed line in Fig. 16a) with the HyperSizer Joints solution. The agreement is excellent near the free edge of the hat flange, while in the web region, where the peel stress is lower, there is some discrepancy. This is expected as the HyperSizer Joints model considers only a bonded doubler (see Fig. 1) and accounts for the presence of the stiffener web only as an effective boundary load. As the stiffener becomes thicker, and less shell-like, one would expect such effective boundary loads to be less representative of a continuum finite element solution.

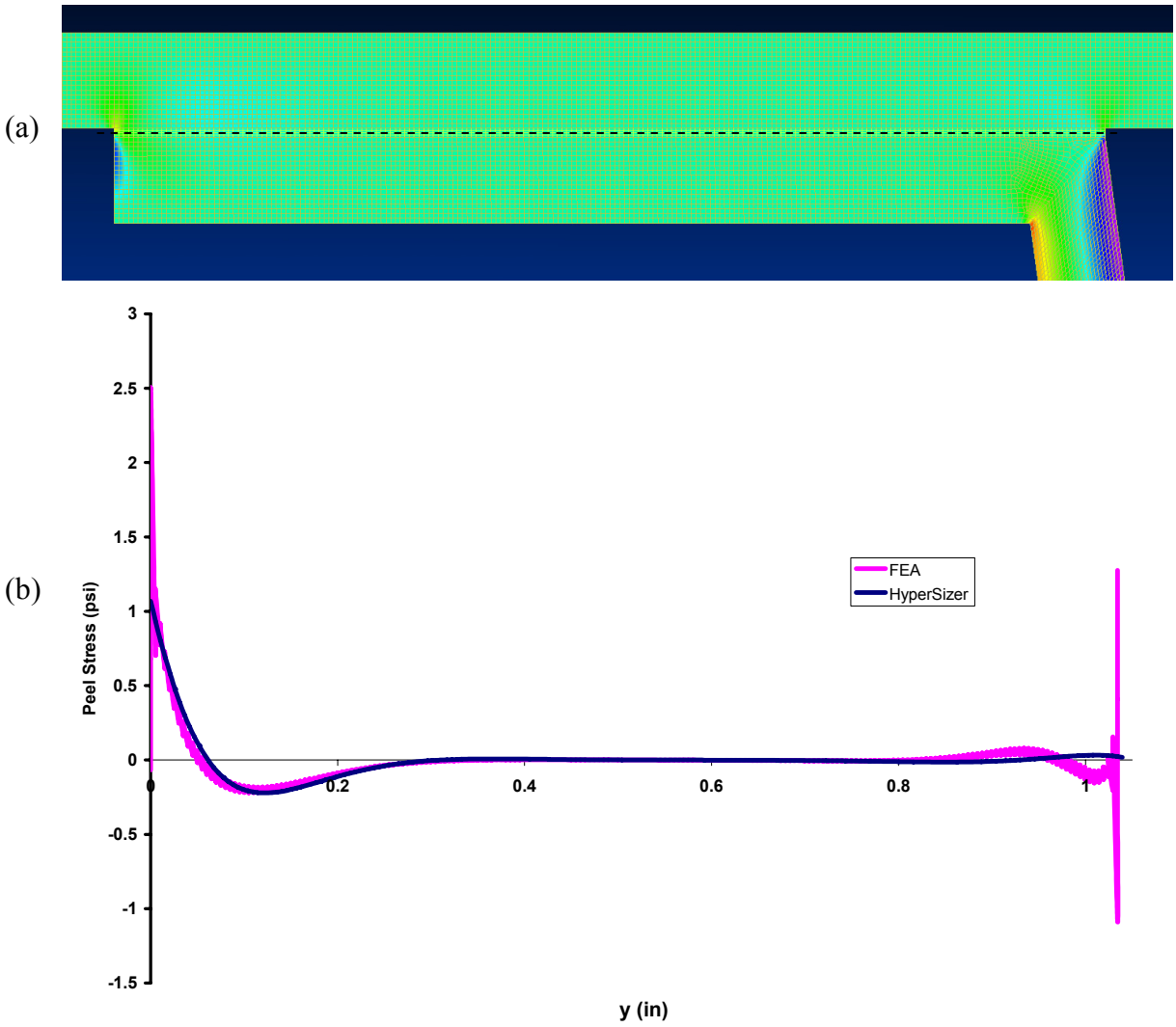

Fig. 16. Peel stress, σ_{zz}, (a) in NASTRAN finite element model (b) plotted along adhesive (dashed line in a), comparing finite element model with HyperSizer Joints.

B. Example 2: Hat Panel Loaded with Applied Moment

The second example problem considers the same hat stiffened panel, but now it is subjected to a moment resultant of -1 in-lb/in. As before, the problem dimensions and material properties are summarized in Fig. 13. Fig. 17 shows a plane strain NASTRAN finite element model of the problem, illustrating the deformed shape. The resulting shear stress, τ_{yz}, within the facesheet to flange joint region is shown in Fig. 18a. Fig. 18b compares the shear stress plotted along the middle of the adhesive in the finite element solution (as indicated by the dashed line) with the HyperSizer Joints adhesive shear stress solution. As shown, the agreement is excellent.

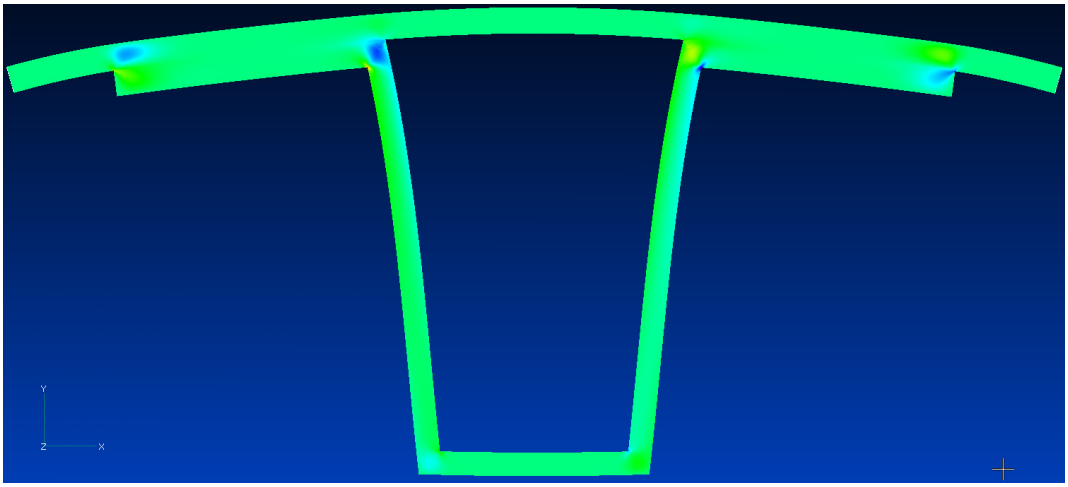

Fig. 17. NASTRAN finite element model deformed shape for example 2 hat stiffened panel.

(a)

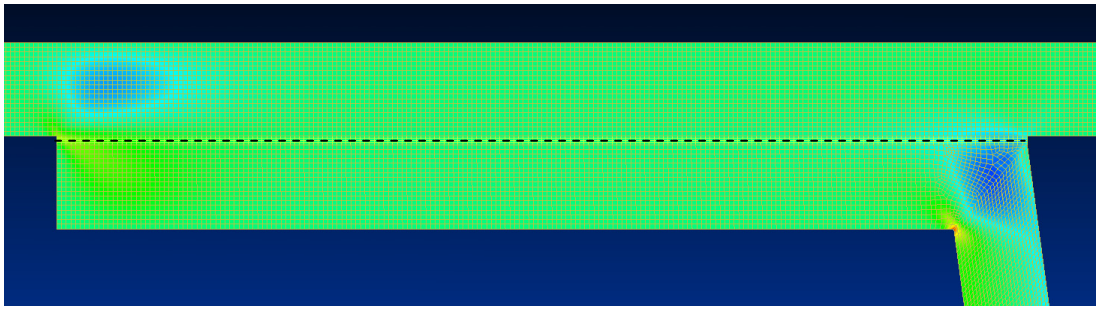

(b)

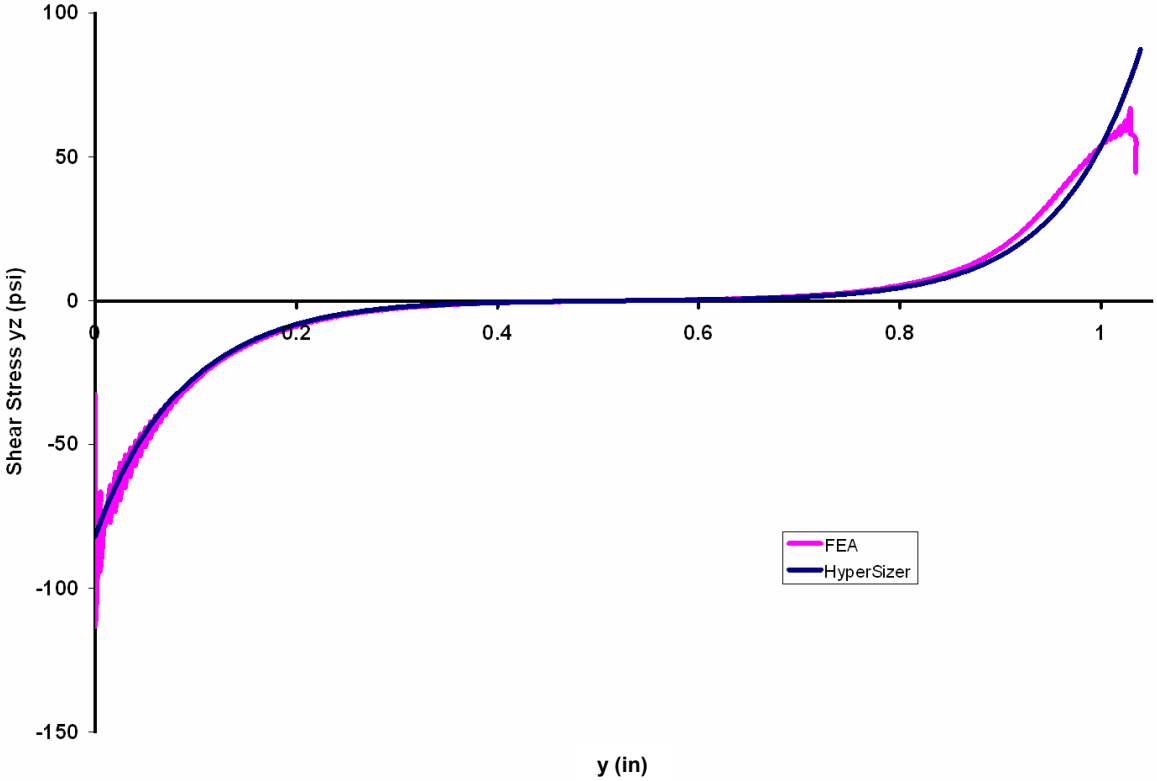

Fig. 18. Shear stress, τ_{yz}, (a) in NASTRAN finite element model (b) plotted along adhesive (dashed line in a), comparing finite element model with HyperSizer Joints.

Fig. 19a shows the peel stress field in the finite element model solution, while Fig. 19b compares the peel stress along the adhesive with the HyperSizer Joints solution. The agreement is excellent near the free edge of the hat flange, while, once again, in the web region, where the peel stress is lower, there is agreement is not as good.

(a)

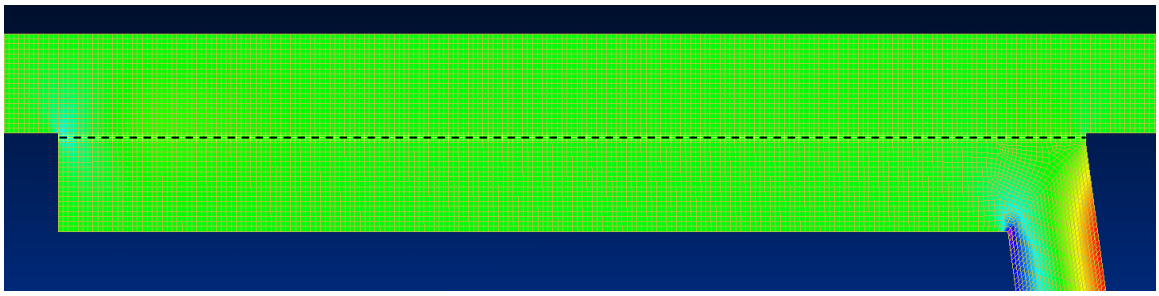

(b)

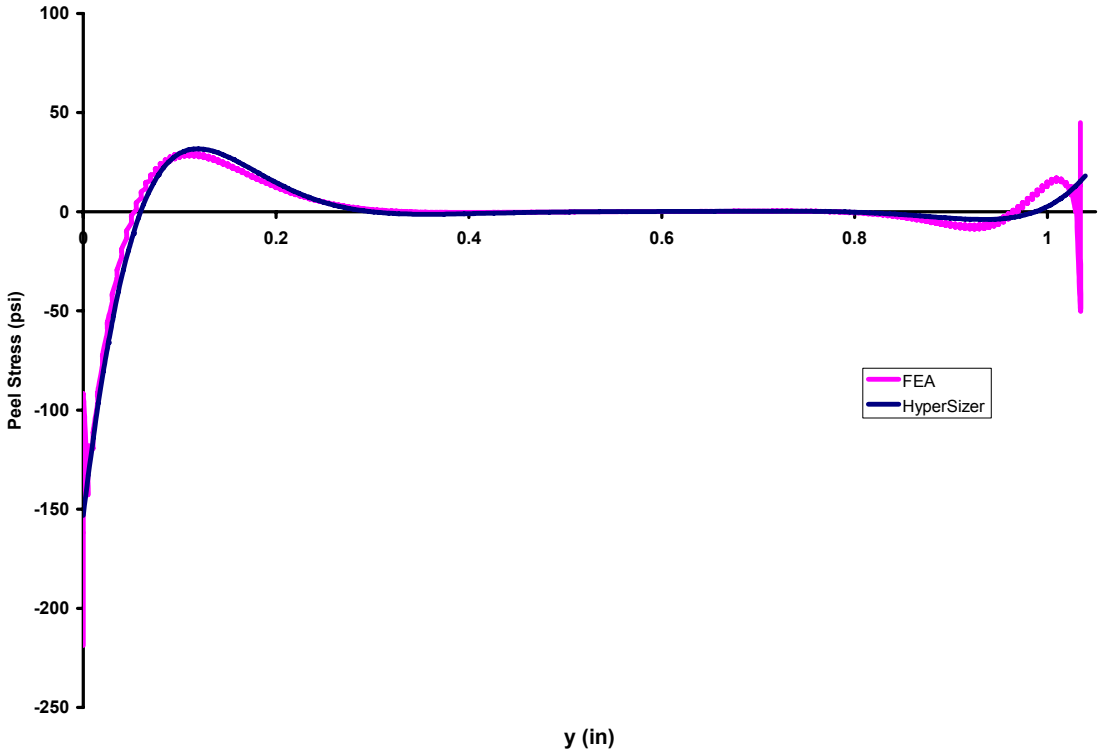

Fig. 19. Peel stress, σ_{zz}, (a) in NASTRAN finite element model (b) plotted along adhesive (dashed line in a), comparing finite element model with HyperSizer Joints.

C. Example 3: Two Sheet Corrugated Panel Loaded with Tensile Force

The third example problem considers a two sheet corrugated stiffened panel subjected to a force resultant of 1 lb/in. As shown in Fig. 20, a two sheet corrugated panel is similar to a hat stiffened panel, with the difference being the fact the two sheet has continuous flanges. The problem dimensions and material properties are summarized in Fig. 20. Fig. 21 shows a plane strain NASTRAN finite element model of the problem, illustrating the deformed shape. The resulting shear stress, τ_{yz}, within the facesheet to flange joint region is shown in Fig. 22a. Fig. 22b compares the shear stress plotted along the middle of the adhesive in the finite element solution with the HyperSizer Joints adhesive shear stress solution. As shown, the agreement is excellent.

Fig. 23a shows the peel stress field in the finite element model solution, while Fig. 23b compares the peel stress along the adhesive with the HyperSizer Joints solution. As shown, there is a significant discrepancy between the HyperSizer Joints solution and the finite element model in this case. While both solutions show a trough and a peak,

the location of these features is not consistent. Again, the approximate way in which the presence of the web is accounted for in the HyperSizer Joints solution (as an effective boundary load) is the likely cause of this discrepancy.

Variable Designs	
	Value
Unit Weight (lb / ft^2)	3.749
Top Face - Thickness (in)	0.1
Core Web - Thickness (in)	0.09
Bottom Face - Thickness (in)	0
Panel - Height (in)	1.747
Corrugation - Spacing (in)	4
Bottom Crown - Width (in)	0.8
Core Web - Angle (degrees)	83.68
Top Flange - Width, hat only (in)	2.855
Top Clear Span - Free Width (in)	0
Top Flange - Thickness (in)	0.09
Bottom Crown - Thickness (in)	0.09

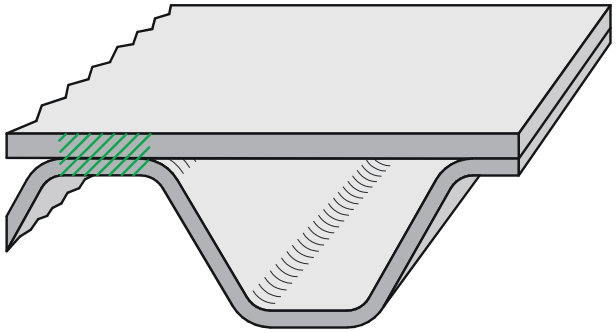

Conceptual Two-Sheet Stiffened Geometry

To-Scale Two-Sheet Stiffened Panel

Facesheet and Hat: Aluminum
E = 10 Msi
G = 3.846 Msi
ν = 0.3

Adhesive: Epoxy
E = .445 Msi
G = .165 Msi
ν = 0.35
thickness = 0.009”

Fig. 20. Example 3 and 4 two sheet corrugated stiffened panel parameters.

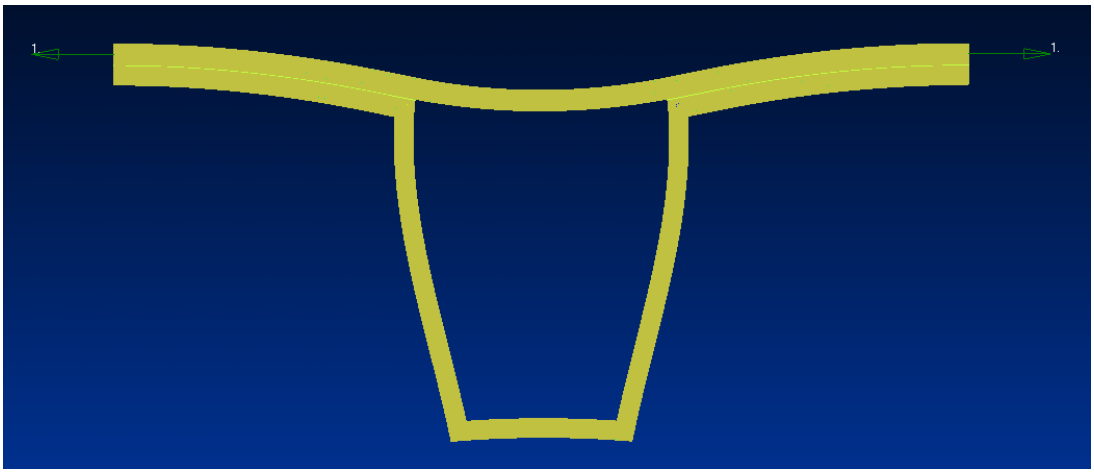

Fig. 21. NASTRAN finite element model deformed shape for example 3 two sheet corrugated stiffened panel.

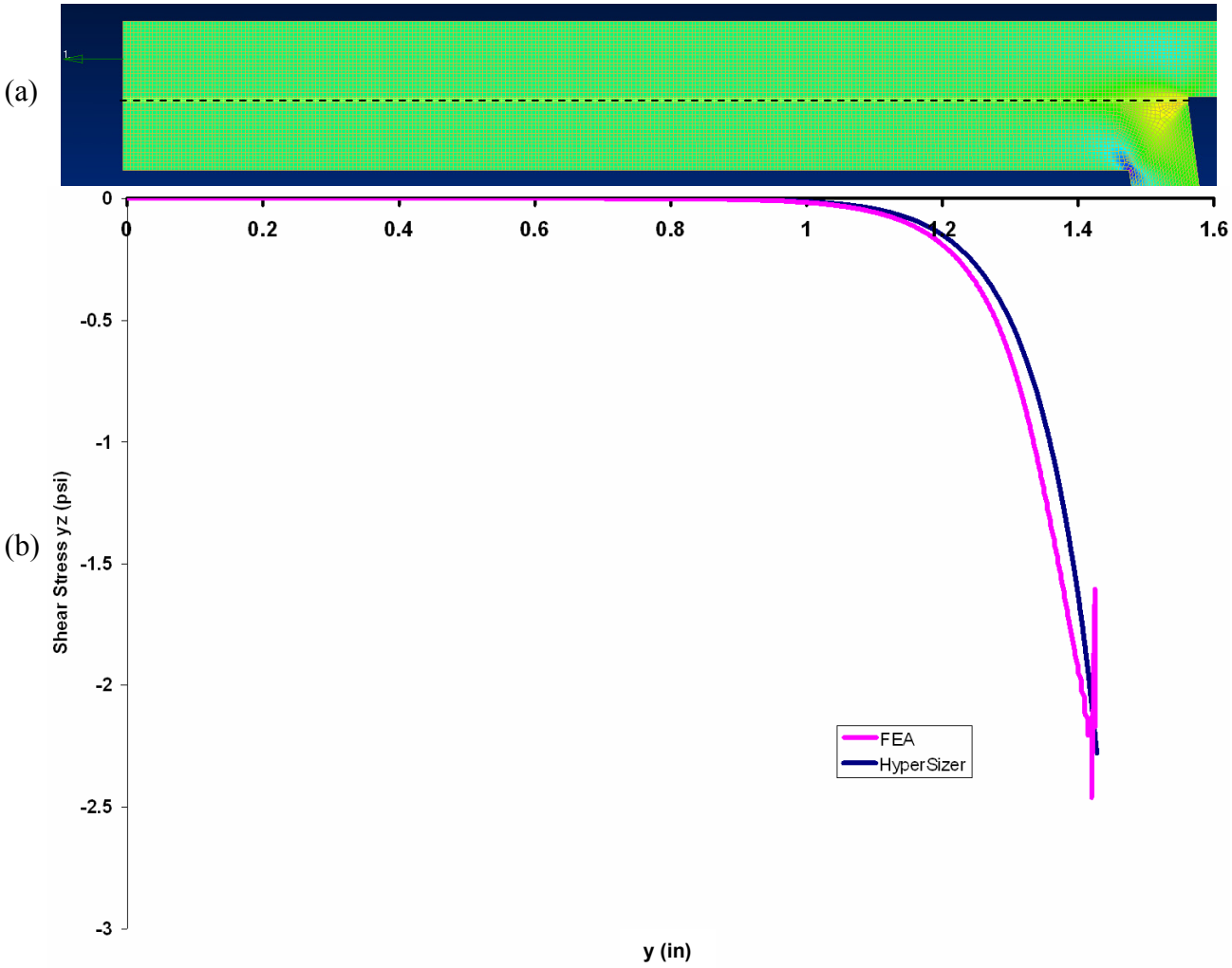

Fig. 22. Shear stress, τ_{yz}, (a) in NASTRAN finite element model (b) plotted along adhesive (dashed line in a), comparing finite element model with HyperSizer Joints.

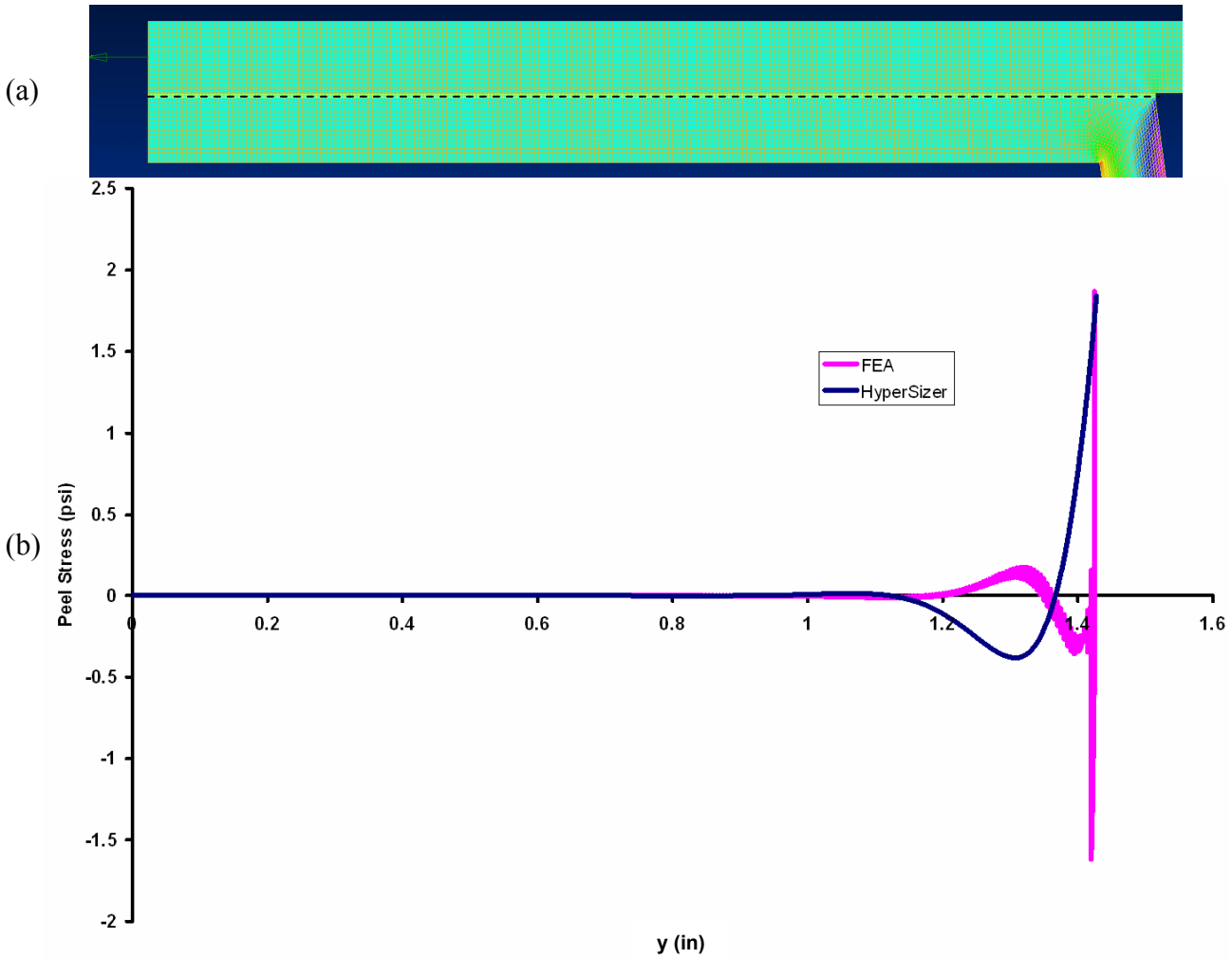

Fig. 23. Peel stress, σ_{zz}, (a) in NASTRAN finite element model (b) plotted along adhesive (dashed line in a), comparing finite element model with HyperSizer Joints.

D. Example 4: Two Sheet Corrugated Panel Loaded with Applied Moment

The fourth example problem considers the same two sheet corrugated stiffened panel, but now it is subjected to a moment resultant of -1 in-lb/in. As before, the problem dimensions and material properties are summarized in Fig. 20. Fig. 24 shows a plane strain NASTRAN finite element model of the problem, illustrating the deformed shape. The resulting shear stress, τ_{yz}, within the facesheet to flange joint region is shown in Fig. 25a. Fig. 25b compares the shear stress plotted along the middle of the adhesive (dashed line in Fig. 25a) in the finite element solution with the HyperSizer Joints adhesive shear stress solution. As shown, the agreement is excellent.

Fig. 27a shows the peel stress field in the finite element model solution, while Fig. 27b compares the peel stress along the adhesive with the HyperSizer Joints solution. The agreement, while better than that exhibited by the two sheet panel subjected to the applied force resultant, still shows some discrepancy with the finite element results.

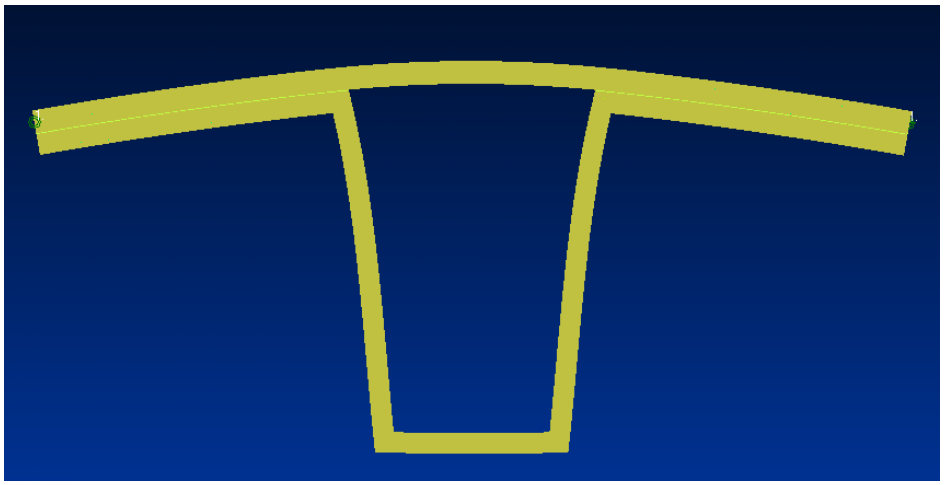

Fig. 24. NASTRAN finite element model deformed shape for example 3 two sheet corrugated stiffened panel.

(a)

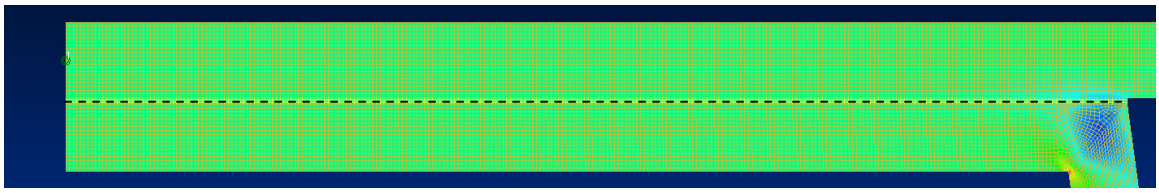

(b)

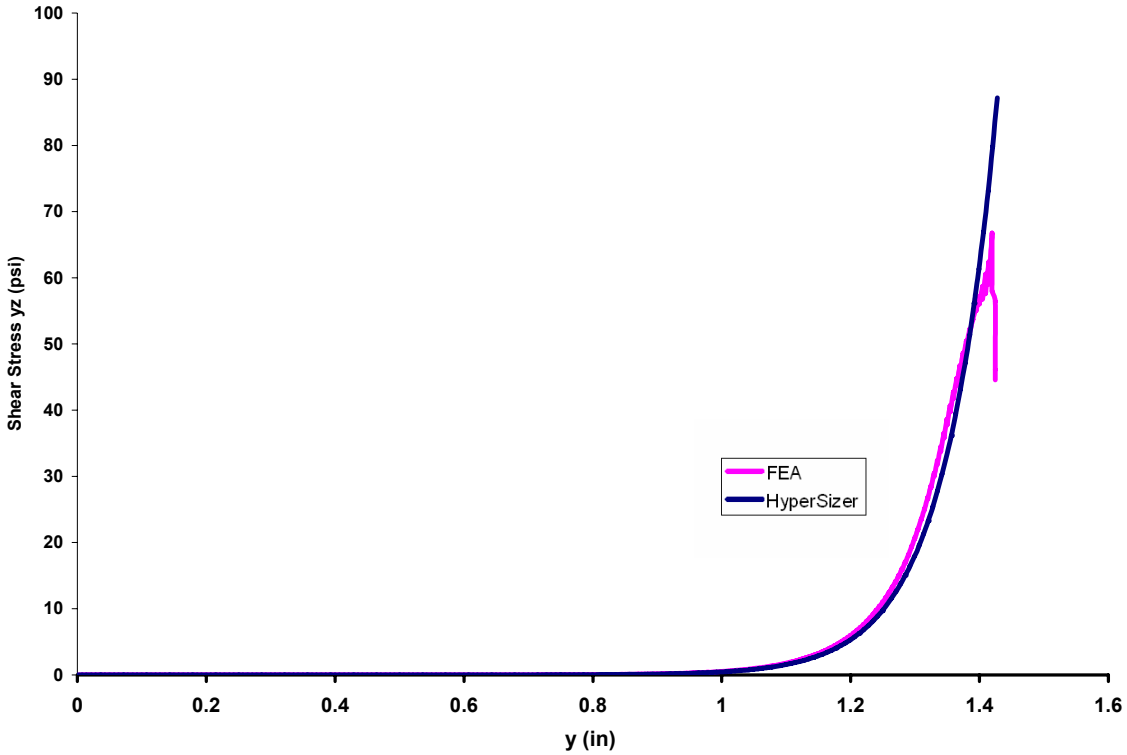

Fig. 25. Shear stress, τ_{yz}, (a) in NASTRAN finite element model (b) plotted along adhesive (dashed line in a), comparing finite element model with HyperSizer Joints.

(a)

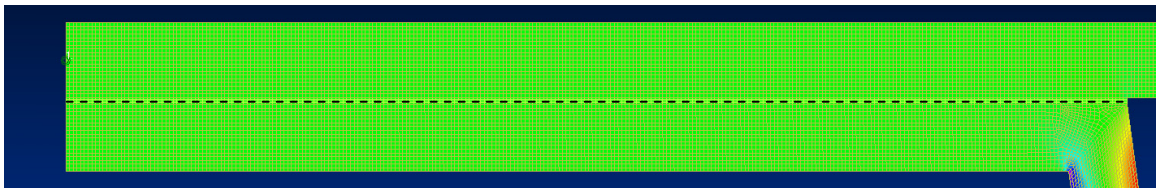

(b)

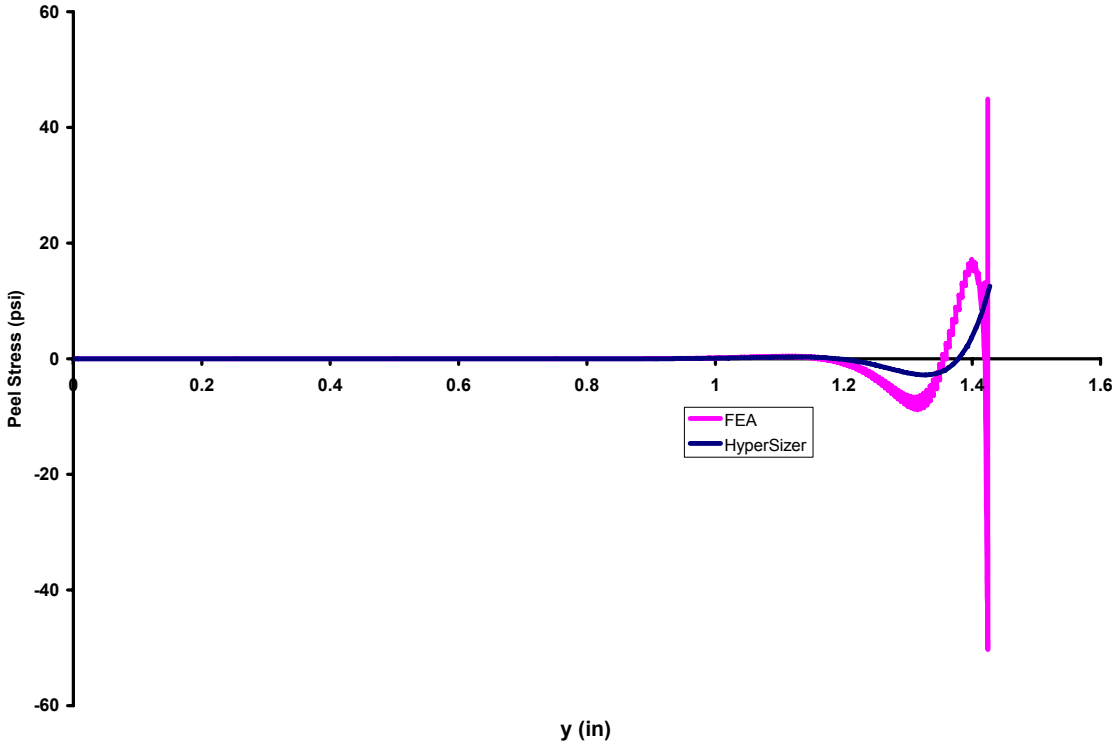

Fig. 26. Peel stress, σ_{zz}, (a) in NASTRAN finite element model (b) plotted along adhesive (dashed line in a), comparing finite element model with HyperSizer Joints

E. Example 5: Composite Hat Stiffened Panel Loaded with Pressure

The final example problem considers a composite hat stiffened panel subjected to a uniform pressure load of 10 psi. The problem dimensions and material properties are summarized in Fig. 27. The chosen composite is a typical graphite/epoxy fabric with all zero plies. This configuration was chosen for the example problem so that the same problem could be solved in a 2-D plane strain FEA. A composite with off-axis plies would require a 3-D finite element model for comparison, which was not constructed for this study. Fig. 28 shows the plane strain NASTRAN finite element solution to this problem, illustrating the deformed shape. For comparison, Fig. 29 shows the deformed shape resulting from the current closed form method. The results for min and max deflection within the facesheet are within about 5% of the FEA result. A comparison between the FEA and the current method for the adhesive shear stress, τ_{yz}, is shown in Fig. 30. Fig. 31 shows a similar comparison of the peel stress in the adhesive. In both cases, the current method shows excellent agreement with the finite element model, even in the vicinity of the web. This better correlation of the peel stress in the web region (compared to the previous results) may be due to the thinner stiffener used in this example. This thinner geometry tends to make the hat stiffener act more like a shell, which in turn makes the effective load boundary conditions used to account for the web more representative.

Variable Designs	
	Value
Unit Weight (lb / ft^2)	1.174
Top Face - Thickness (in)	0.098
Core Web - Thickness (in)	0.028
Bottom Face - Thickness (in)	0
Panel - Height (in)	1.747
Corrugation - Spacing (in)	4
Bottom Crown - Width (in)	0.8
Core Web - Angle (degrees)	82.24
Top Flange - Width, hat only (in)	2.079
Top Clear Span - Free Width (in)	0
Top Flange - Thickness (in)	0.028
Bottom Crown - Thickness (in)	0.028

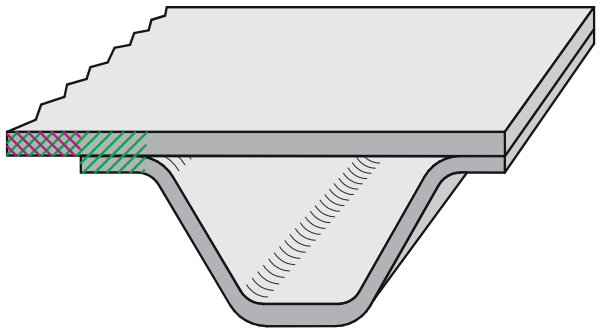

Conceptual Hat Stiffened Panel Geometry

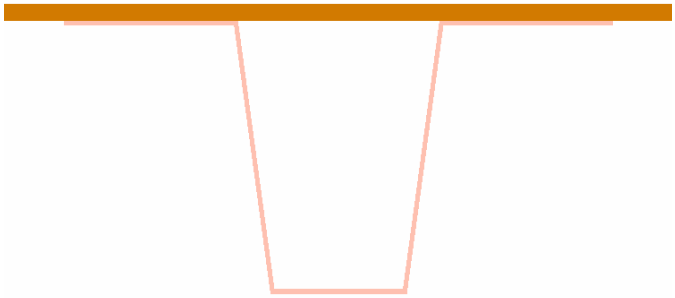

To-Scale Composite Hat Stiffened Panel

Facesheet and Hat: Graphite Epoxy Fabric
E_1 = 11 Msi; E_2 = 10.1 Ms
$G_{12} = G_{13} = G_{23}$ = 0.76 Msi
ν_{12} = 0.0363
Ply Thickness = 0.014"

Facesheet Layup
7 Plies; $[0_7]$ – Total Thickness = 0.098"

Hat Flange, Web, Crown Layup
2 Plies; $[0_2]$ – Total Thickness = 0.028"

Loading
Pressure = 10 psi

Adhesive: Epoxy
E = .445 Msi
G = .165 Msi
ν = 0.35
thickness = 0.009”

Fig. 27. Example 5 composite fabric corrugated stiffened panel parameters.

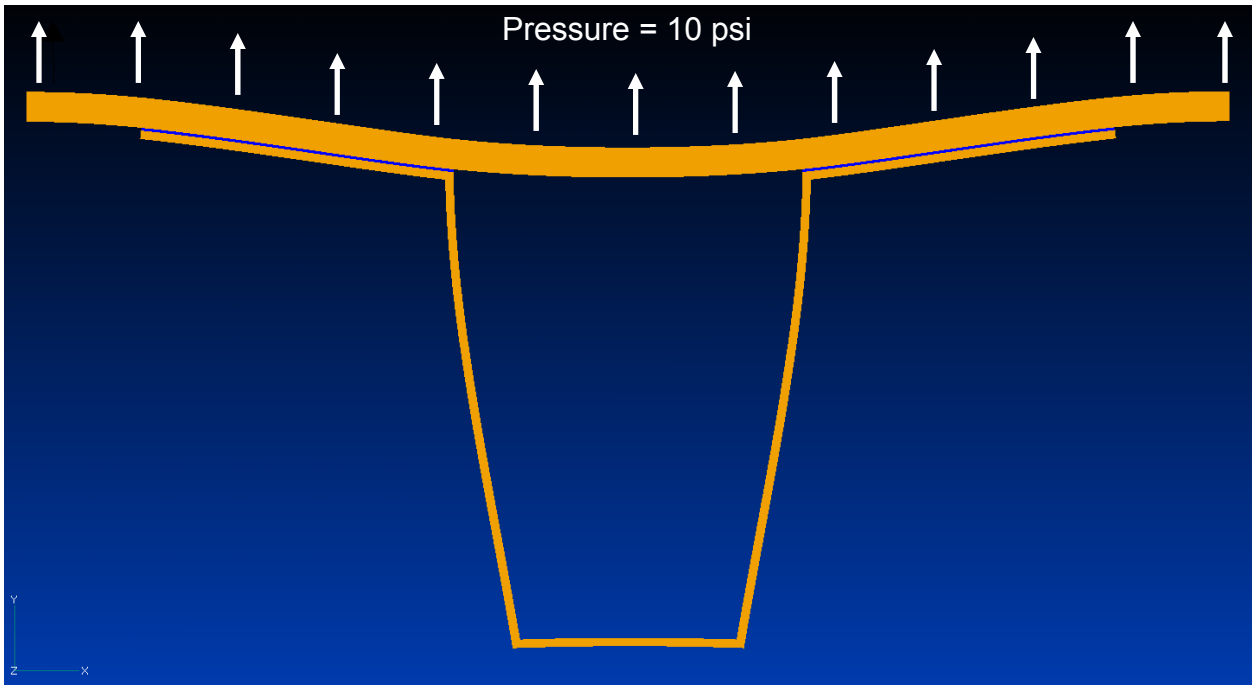

Fig. 28. NASTRAN finite element model deformed shape for example 5 composite hat stiffened panel with applied pressure.

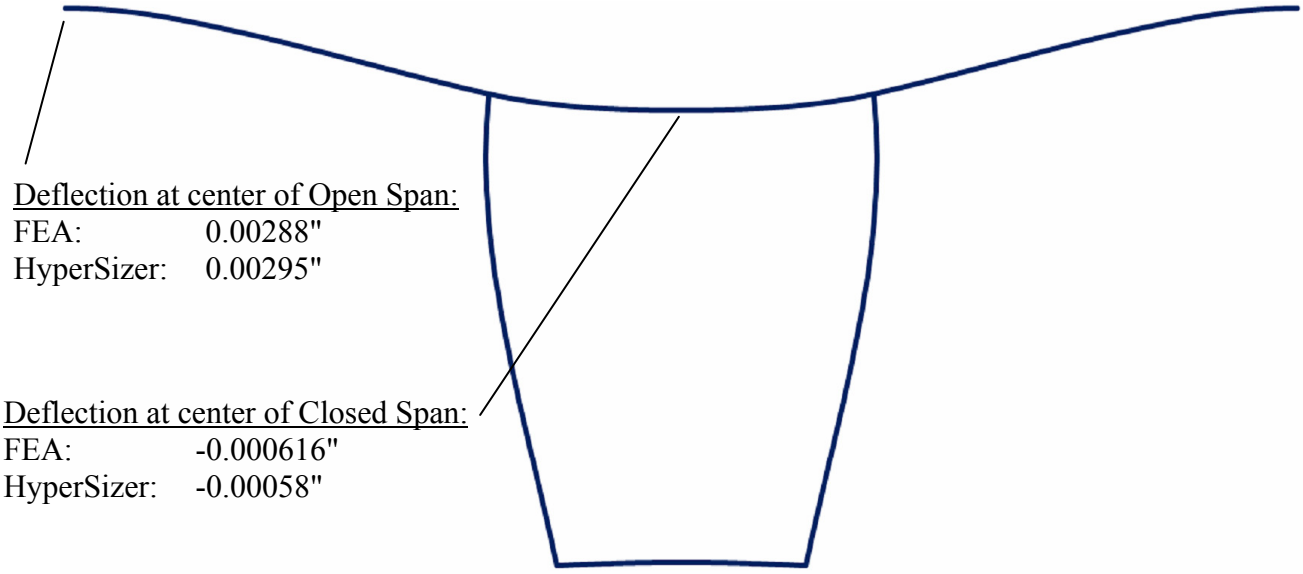

Fig. 29. Deformed shape from the current closed form formulation (scale factor different than in Fig. 28).

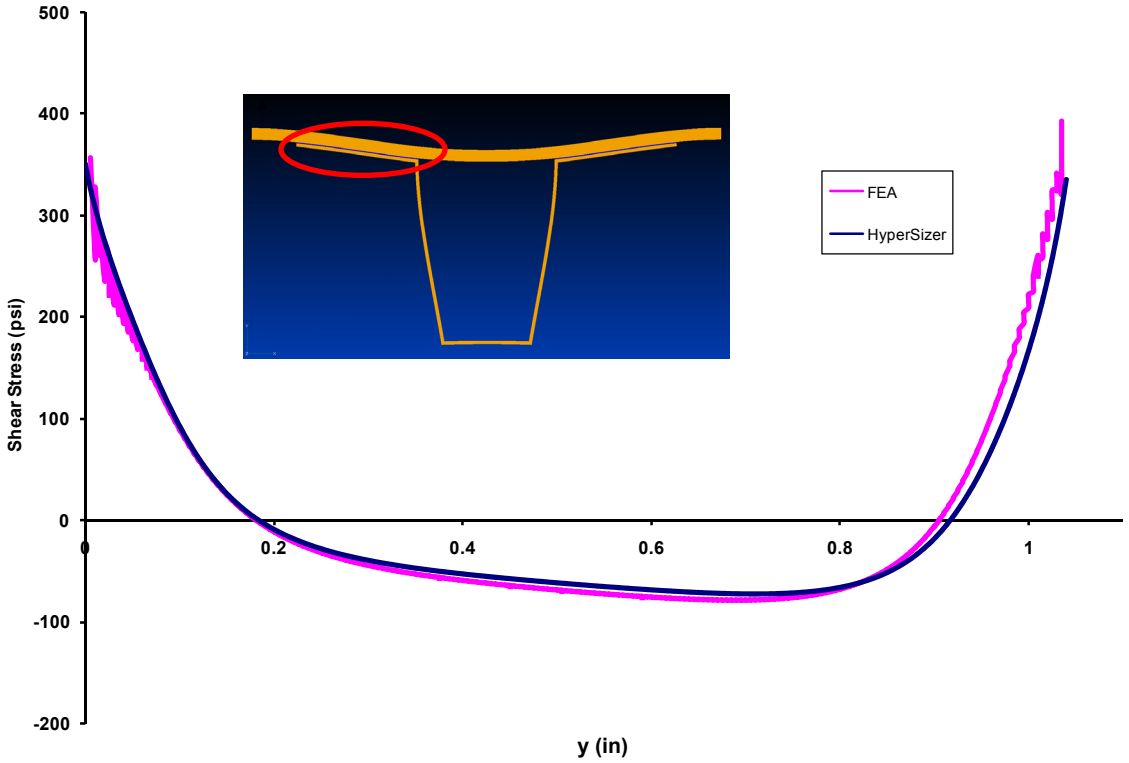

Fig. 30. Shear stress, τ_{yz}, plotted along adhesive, comparing finite element model with HyperSizer Joints.

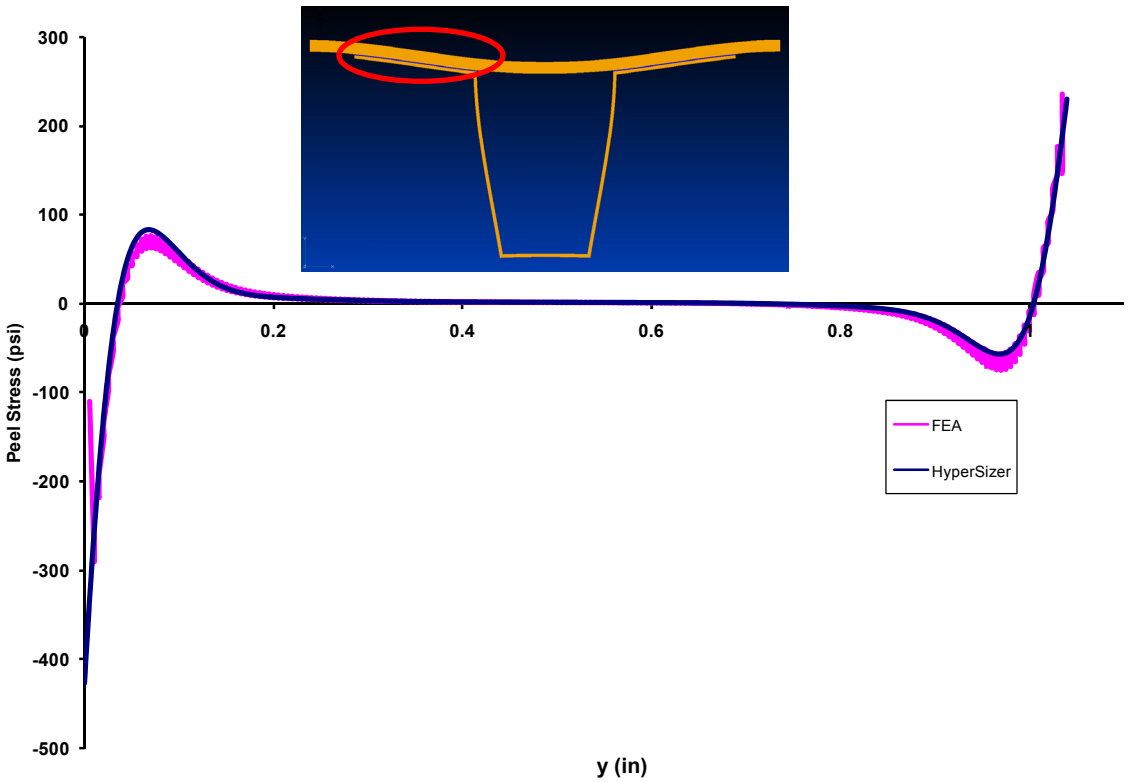

Fig. 31. Peel stress, σ_{zz}, plotted along adhesive, comparing finite element model with HyperSizer Joints.

V. Conclusion

A method for the rapid analysis of facesheet to flange bonded joints in composite corrugated panels has been developed. The bonded joint analysis is based on the HyperSizer Joints methodology[4-9], which is an analytical approach for determining the stress fields arising in the joint adherends and adhesive. In order to obtain the boundary loads specific to a given corrugated panel needed for application within the HyperSizer Joints analysis, a beam analogy model has been developed. This beam analogy model allows for a moment resultant and normal and shear force resultants, as well as pressure, to be applied, the magnitudes of which (for instance) can be obtained from a global finite element loads model. Thus, starting on this global scale, the loads can be localized and applied to the corrugated panel flange to facesheet bonded joint, and the local ply-level in-plane and interlaminar stress fields can be calculated. Ply-level margins of safety can then be determined based on ply-level failure criteria, and the viability of a given corrugated panel design can be evaluated. This new capability has been incorporated within the HyperSizer Structural Sizing Software[1], enabling a new level of fidelity in the software's corrugated panel preliminary design capability.

Results comparing the method to finite element analysis for monolithic and composite hat stiffened and two sheet corrugated panels were presented. It was shown that the method predicts joint adhesive peel stresses that match well with the finite element result in most cases. The predicted joint adhesive shear stresses match very well with the finite element results in all cases examined. The main discrepancy between the method and the finite element peel stress results occurred at the point where the web intersects the flange at an angle (see Fig. 3). This angle intersection geometry is accurately captured in the finite element model, while in the joint analysis, an effective boundary load is applied at this point and the detailed local stress field induced by the web angle within the continuum finite element analysis is not captured. It is thus expected that the predicted stress fields would be more approximate in this region. In sum, however, the method has been shown to give quite accurate results in an efficient closed form suitable for structural optimization problems in which thousands of potential corrugated panel configurations must be considered rapidly.

References

[1] Collier Research Corporation, HyperSizer Structural Sizing Software, Hampton, VA, www.hypersizer.com, 2008.

[2] Mortensen, F., "Development of Tools for Engineering Analysis and Design of High-Performance FRP-Composite Structural Elements" Ph.D. Thesis, Institute of Mechanical Engineering, Aalborg University (Denmark), Special Report no. 37, 1998.

[3] Mortensen, F. and Thomsen, O.T., "Analysis of Adhesive Bonded Joints: A Unified Approach," *Composites Science and Technology*, Vol. 62, 2002, pp. 1011-1031.

[4] Zhang, J., Bansal, Y., Bednarcyk, B.A., Collier, C.S., and Pindera, M.-J. "Analysis of Adhesively Bonded Composite Joints Using a Higher-Order Theory" in *Proc. 45th AIAA/ASME/ASCE/AHS/ASC Structures, Structural Dynamics, and Materials Conference*, April, 2004, Palm Springs, California.

[5] Zhang, J., Bednarcyk, B.A., Collier, C., Yarrington, P., Bansal, Y., and Pindera, M.-J., "3D Stress Analysis of Composite Bonded Joints," Proc. *46th AIAA/ASME/ASCE/AHS/ASC Structures, Structural Dynamics, and Materials Conference*, April, 2005, Austin, Texas.

[6] Yarrington, P.W., Zhang, J., Collier, C.S., and Bednarcyk, B.A., "Failure Analysis of Adhesively Bonded Composite Joints," in *Proc. 46th AIAA/ASME/ASCE/AHS/ASC Structures, Structural Dynamics, and Materials Conference*, April, 2005, Austin, Texas.

[7] Bednarcyk, B.A., Zhang, J., Collier, C.S., Bansal, Y., and Pindera, M.-J., "Analysis Tools for Adhesively Bonded Composite Joints, Part I: Higher-Order Theory," *AIAA Journal*, Vol. 44, No. 1, 2006, pp. 171-180.

[8] Zhang, J., Bednarcyk, B.A., Collier, C.S., Yarrington, P.W., Bansal, Y., and Pindera, M.-J., "Analysis Tools for Adhesively Bonded Composite Joints, Part II: Unified Analytical Theory," *AIAA Journal*, Vol 44, No. 8, 2006, pp. 1709-1719.

[9] Yarrington, P.W., Collier, C.S., and Bednarcyk, B.A., "Failure Analysis of Adhesively Bonded Composite Joints via the Virtual Crack Closure Technique," Proc. *47th AIAA/ASME/ASCE/AHS/ASC Structures, Structural Dynamics, and Materials Conference*, April, 2006, Newport, Rhode Island.

[10] ABAQUS, Inc., *ABAQUS Analysis User's Manual*, Vol. 4, Version 6.5, 2004.

[11] Camanho, P.P. and Davila, C.G., "Mixed-Mode Decohesion Finite Elements for the Simulation of Delamination in Composite Materials" NASA/TM-2002-211737, 2002.

[12] Beer, F.P. and Johnston, E.R., *Mechanics of Materials*, McGraw-Hill, New York, 1981.